The time scale of shallow convective self-aggregation in large-eddy simulations is sensitive to numerics

Martin Janssens[1], Jordi Vilà-Guerau de Arellano[2], Chiel C. van Heerwaarden[1], Bart van Stratum[1], Stephan R De Roode[3], Pier Siebesma[4], and Franziska Glassmeier[5]

[1]Wageningen University & Research
[2]Wageningen University Research
[3]Delft University of Technology
[4]TU Delft
[5]TU Delft

November 25, 2022

Abstract

Numerical simulations of the tropical mesoscales often exhibit a self-reinforcing feedback between cumulus convection and shallow circulations, which leads to the self-aggregation of large cloud structures. We investigate whether this basic feedback can be adequately captured by large-eddy simulations (LESs). To do so, we simulate the non-precipitating, cumulus-topped boundary layer of the canonical 'BOMEX'; case over a range of numerical settings in two models. Since the energetic convective scales underpinning the self-aggregation are only slightly larger than typical LES grid spacings, aggregation timescales do not converge even at rather high resolutions (less than 100m). Therefore, high resolutions or improved unresolved scales models may be required to faithfully represent certain forms of trade-wind mesoscale cloud patterns and self-aggregating deep convection in large-eddy and cloud-resolving models, and to understand their significance relative to other processes that organise the tropical mesoscales.

The time scale of shallow convective self-aggregation in large-eddy simulations is sensitive to numerics

Martin Janssens[1,2], Jordi Vilà-Guerau de Arellano[1], Chiel C. van Heerwaarden[1], Bart J.H. van Stratum[1], Stephan R. de Roode[2], A. Pier Siebesma[23], Franziska Glassmeier[2]

[1]Meteorology & Air Quality department, Wageningen University, Wageningen, Netherlands
[2]Geoscience & Remote Sensing department, Delft University of Technology, Delft, Netherlands
[3]Royal Netherlands Institute of Meteorology, De Bilt, Netherlands

Key Points:

- In large-eddy simulations, sub-kilometre scale cumulus convection self-organises into mesoscale structures through shallow circulations
- The aggregation time-scale does not converge with model resolution for typical discretisation choices.
- Numerical representations of the tropical mesoscales may require finer model resolutions than previously thought

Corresponding author: Martin Janssens, `martin.janssens@wur.nl`

Abstract

Numerical simulations of the tropical mesoscales often exhibit a self-reinforcing feedback between cumulus convection and shallow circulations, which leads to the self-aggregation of large cloud structures. We investigate whether this basic feedback can be adequately captured by large-eddy simulations (LESs). To do so, we simulate the non-precipitating, cumulus-topped boundary layer of the canonical 'BOMEX' case over a range of numerical settings in two models. Since the energetic convective scales underpinning the self-aggregation are only slightly larger than typical LES grid spacings, aggregation timescales do not converge even at rather high resolutions (<100m). Therefore, high resolutions or improved unresolved scales models may be required to faithfully represent certain forms of trade-wind mesoscale cloud patterns and self-aggregating deep convection in large-eddy and cloud-resolving models, and to understand their significance relative to other processes that organise the tropical mesoscales.

Plain Language Summary

The most detailed models of our atmosphere frequently have their clouds spontaneously organise into large clusters. Small clouds (less than a kilometre in size) seem to play an important role in such "self-aggregation". However, even in detailed models small clouds are hard to adequately capture: Typically, they must resolve such clouds using less than 10 pixels, thus requiring additional, lower-accuracy "unresolved-scales" models for cloudy motions smaller than this resolution. Here, we show that merely varying the resolution of several state-of-the-art atmospheric models has an effect on how quickly they predict the self-aggregation of clouds to occur, even when many complex, uncertain processes are removed from the problem. We hypothesise that this is because several fundamental assumptions of our unresolved scales models are commonly violated in simulations of self-aggregating clouds. To help work out how important self-aggregation is in the real world, models of the phenomenon may therefore require higher numerical resolutions than previously thought.

1 Introduction

A striking feature of idealised simulations of the tropical atmosphere in radiative-convective equilibrium (RCE) is the spontaneous aggregation of their column-integrated moisture and convection into large clusters (Bretherton et al., 2005; Muller & Held, 2012). Many mechanisms have been proposed to explain this, including the collision and convective triggering of horizontally expanding and colliding cold pools of evaporated precipitation (Tompkins, 2001; Böing, 2016; Haerter, 2019) and gravity wave-convection interactions (Yang, 2021). Yet, perhaps the strongest consensus is on the importance of shallow circulations (Shamekh et al., 2020; Muller et al., 2022), configured to transport moisture from dry to moist columns.

These circulations can be traced to differential, radiative cooling between moist regions, which trap outgoing longwave radiation in their moisture-rich lower atmosphere and under high clouds, and dry regions, which more readily radiate their thermal energy to space (Muller & Held, 2012). Such heating anomalies give rise to ascent in moist columns and descent in dry columns, and may be framed as moisture-radiation instabilities (Emanuel et al., 2014; Beucler & Cronin, 2016) with negative moist gross stability (Bretherton et al., 2005; Raymond et al., 2009). However, the circulations may also be reinforced by turbulent mixing at cloud edges, which deposits moisture in the free troposphere and thus raises the livelihood and vigour of any subsequent convection; differential convection may then itself result in a net ascent of moist, convecting regions and descent in dry, non-convecting regions (Grabowski & Moncrieff, 2004; Tompkins & Semie, 2017). Interactions between these radiative and convective feedbakcs appear important, and their relative significance is debated (Beucler et al., 2018; Kuang, 2018).

Rooting deep convective self-aggregation in shallow circulations implicitly underlines the importance of shallow convection in developing and maintaining them. Bretherton et al. (2005); Muller and Held (2012) make this connection explicit; they show that shallow convection in dry regions exports moist static energy, an appropriate energetic measure of the moisture, to moist, deep convective regions. If one removes cold-pool feedbacks, the shallow circulation is even more tightly coupled to the effects of shallow, non-precipitating convection. In such situations, self-aggregation occurs also on smaller domains (Jeevanjee & Romps, 2013) and without requiring radiative feedbacks (Muller & Bony, 2015).

Interestingly, shallow cumulus convection under typical trade-wind conditions also self-organises into clusters much larger than that of individual cumuli (e.g. Narenpitak et al., 2021). Bretherton and Blossey (2017); Janssens et al. (2022) attribute such aggregation to the convective feedback: Shallow circulations driven by anomalous latent heating in shallow cumulus transport moisture from dry to moist regions in the absence of radiative or precipitating heterogeneity. If integrated over sufficiently long time periods, simulations of this mechanism aggregate enough moisture into their moist regions to transition into deep, organised convection (see also Vogel et al., 2016). These studies likely describe the confluence of shallow convective instability and the deep convective instabilities described by Jeevanjee and Romps (2013); Muller and Bony (2015), and grounds the latter in the former.

These paragraphs serve to illustrate that an extensive body of work may rely rather strongly on how well the numerical models used to simulate convective self-aggregation represent shallow convection. To remain tractable when running on domains of $O(1000)$ km, numerical simulations of self-organisation often employ rather coarse grid spacings (usually greater than 1 km). At such grid spacings, shallow convection, whose energetic scales themselves lie around 1 km, are at best barely resolved, and at worst parameterised.

This is relevant, since convective self-aggregation is sensitive to numerical settings and parameterisations in cloud-resolving simulations of deep convection (Muller & Held, 2012; Wing et al., 2020) and large-eddy simulations (LESs) of cold pool-driven pattern formation in shallow convection (Seifert & Heus, 2013). One may therefore wonder if the self-aggregation of non-precipitating cumulus is subject to similar sensitivities, whether this matters when attempting to interpret numerical simulations of deep convective self-aggregation and ultimately how much the phenomenon bears on reality. This motivates us to ask the question: Can we consistently represent convective self-aggregation in its most basic form - shallow, non-precipitating cumulus convection - in LES?

Guided by this question, we revisit a classical case of non-precipitating shallow cumulus convection and simulate it on a mesoscale domain in several numerical configurations (section 2). We then summarise the feedback mechanism discussed by Bretherton and Blossey (2017); Janssens et al. (2022) that drives the self-aggregation in these simulations (section 3). Next, we demonstrate the multiscale nature of the feedback: Small, cumulus-scale processes drive moisture variability at scales an order of magnitude larger (section 4). This renders it sensitive to three choices that govern the effective resolution of finite-volume-based LES: grid spacing, advection scheme and unresolved scales model (section 5). We discuss the implications of these findings for modelling studies of shallow and deep convective self-aggregation and their potential parameterisation in section 6, before summarising in section 7.

2 Numerical Simulations

2.1 Case study

Our study concerns a set of numerical experiments of the "undisturbed period" during the Barbados Oceanographic and Meteorological Experiment (BOMEX), as intro-

duced to the LES modelling community by Siebesma and Cuijpers (1995). We concentrate on BOMEX because it represents the simplest imaginable setting of shallow cumulus convection, simulating only moist thermodynamics and boundary-layer turbulence.

Three assumptions made in the composition of our case deserve mention here. First, in lieu of representing spatial and temporal variability in i) the large-scale subsidence, ii) horizontal wind and iii) surface fluxes of heat and moisture, we parameterise such larger-scale and boundary forcings with profiles that vary only in height. Second, we do not locally calculate radiative heating rates, instead approximating them with a slab-averaged cooling. Third, we explicitly ignore the formation and impact of precipitation. We will therefore suppress aggregation that is forced on our cloud-field by vertical motions of a scale larger than our domain, such as those imposed in the simulations conducted by Narenpitak et al. (2021) and observed by George et al. (2022), by radiation heterogeneity (Klinger et al., 2017) and by cold-pool dynamics (e.g. Seifert & Heus, 2013; Seifert et al., 2015; Anurose et al., 2020; Lamaakel & Matheou, 2022) respectively, all of which appear important pathways to develop the mesoscale cumulus patterns observed in nature.

We justify the neglect of these processes by noting that they are not necessary for large, aggregated cumulus structures to develop (Bretherton & Blossey, 2017). Instead, they accelerate and modulate an internal mechanism that also occurs without them. This feedback is intrinsic to moist, shallow convection (Janssens et al., 2022), and its sensitivity to resolution is most clearly exposed by only studying this aspect. We will return briefly to this discussion in section 6.

2.2 Numerical model

We perform simulations with two models: The Dutch Atmospheric Large Eddy Simulaton (DALES, Heus et al., 2010; Ouwersloot et al., 2017) and MicroHH (Van Heerwaarden et al., 2017). Both models attain a numerical representation of the atmospheric state on a staggered grid by solving filtered, finite difference approximations of the conservation equations of mass, momentum, and scalars in the anelastic approximation:

$$\frac{\partial}{\partial x_j}\left(\rho_0 u_j\right) = 0 \tag{1}$$

$$\frac{\partial u_i}{\partial t} = -\frac{1}{\rho_0}\frac{\partial}{\partial x_j}\left(\rho_0 u_i u_j\right) - \frac{\partial \pi'}{\partial x_i} + \frac{g}{\overline{\theta_v}}\left(\theta_v - \overline{\theta_v}\right)\delta_{i3} - \frac{\partial \tau_{ij}}{\partial x_j} + S_{u_i} \tag{2}$$

$$\frac{\partial \chi_i}{\partial t} = -\frac{1}{\rho_0}\frac{\partial}{\partial x_j}\left(\rho_0 u_j \chi_i\right) - \frac{\partial R_{u_j,\chi_i}}{\partial x_j} + S_{\chi_i}, \tag{3}$$

In these equations, $u_i \in \{u, v, w\}$ are the three (grid-filtered) components of velocity, $\chi_i \in \{\theta_l, q_t\}$ is a generic scalar whose set contains at least the total specific humidity q_t and liquid-water potential temperature, approximated as

$$\theta_l \approx \theta - \frac{L_v}{c_p \Pi} q_l. \tag{4}$$

where θ is the (dry) potential temperature, L_v is the latent heat of vaporisation, c_p is the specific heat of dry air at constant pressure, q_l is the liquid water specific humidity and

$$\Pi = \left(\frac{p}{p_0}\right)^{\frac{R_d}{c_p}} \tag{5}$$

is the Exner function, where R_d is the gas constant of dry air and p is the reference pressure profile. The corresponding reference density is ρ_0, π' are fluctuations of modified

pressure around p, g is gravitational acceleration, θ_v is the virtual potential temperature whose slab-mean is represented by an overbar, S_{u_i} and S_{χ_i} denote momentum and scalar sources, and τ_{ij} and R_{u_j,χ_i} are the residual fluxes of momentum and scalars that result from filtering the equations (the Sub-Filter Scale (SFS) fluxes). These fluxes are approximated with a traditional eddy viscosity model, which explicitly assumes the filtering to take place at a scale where diffusion of the resolved flow approximates the net dissipation of homogeneous, isotropic turbulence; it must be significantly smaller than the energy-containing scales of the simulation:

$$\tau_{ij} \approx -K_m \left(\frac{\partial u_i}{\partial x_j} + \frac{\partial u_j}{\partial x_i} \right) \tag{6}$$

$$R_{u_j,\chi_i} \approx -K_h \frac{\partial \chi_i}{\partial x_j} \tag{7}$$

These approximations introduce modelling errors which can be expected to influence the large, resolved scales when their requirements are not met.

The main differences between DALES and MicroHH reside in their model for the eddy diffusivities K_m and K_h: DALES uses a one-equation closure for the turbulent kinetic energy e (Deardorff, 1973) subject to Deardorff (1980)'s stability correction; MicroHH employs a stability-corrected Lilly-Smagorinsky model (Lilly, 1968). Both models estimate K_m and K_h through a mixing length λ associated with the grid-scale filter:

$$\lambda = f\left(\Delta\right), \tag{8}$$

$$\Delta = \left(\Delta x \Delta y \Delta z\right)^{\frac{1}{3}}, \tag{9}$$

where f subsumes the stability correction, which diminishes the eddy diffusivities in stably stratified grid cells, and where Δ assumes the grid spacing is isotropic, which is an assumption we will violate. Note that Δ also sets the discretisation error in the model's spatial gradients for a finite difference scheme of a given order; these errors will interact non-trivially with the modelling error made by the approximations above.

2.3 Experiments

We base our analysis on 8 simulations of BOMEX that are set up in the configuration reported by Siebesma et al. (2003), except for their computational grid, integration time and advection scheme. To support mesoscale fluctuations with little influence from the finite domain size, the cases are run on domains with horizontal length $L =$ 102.4 km, a height of 10 km, for 36 hours. The vertical grid spacing $\Delta z = 40$ m up to 6 km, and is stretched by 1.7% per level above this height. To investigate how the development of mesoscale fluctuations is sensitive to numerics, we vary the horizontal grid spacing $\Delta x = \Delta y \in [50, 100, 200]$ m. At their coarsest spacing, our grid cells attain rather high aspect ratios. Such anisotropic grids are commonly used in large-domain LES of shallow cumulus convection (e.g. Vogel et al., 2016; Klinger et al., 2017; Bretherton & Blossey, 2017; Janssens et al., 2022), although the isotropic filter length scale λ consequently overestimates the vertical length scale required from the SFS model, and underestimates the horizontal length scale (de Roode et al., 2022). As will become clear in section 5, we will be particularly concerned with the underestimation of the horizontal length scale. Therefore, we also run the DALES simulations at $\Delta x = 200$ m with $\Delta = 200$ m.

All cases are run with a variance-preserving, second order central difference scheme to represent advective transfer, while the coarsest two DALES simulations are additionally run using a fifth order, nearly monotonic scheme (Wicker & Skamarock, 2002). This

Table 1. Differences in numerical configurations of BOMEX simulations. e refers to the one-equation turbulence kinetic energy SFS model (Deardorff, 1973); SL refers to the Smagorinsky-Lilly model (Lilly, 1968). Advection schemes are either $O(2)$ central differences (a2), or the $O(5)$ scheme by Wicker and Skamarock (2002) (a5). 'fiso' refers to coarsening the filter as if it were isotropically increasing with the horizontal grid spacing, while 'nocorr' denotes a run with Deardorff (1980)'s stability correction turned off.

Abbreviation	Model	Δx	SFS model	Advection scheme	Δ
D1	DALES	200	e	$O(2)$ a2	117
D2	DALES	200	e	$O(5)$ a5	117
D3	DALES	200	e	$O(2)$ a2	200, fiso
D4	DALES	100	e	$O(2)$ a2	73.7
D5	DALES	100	e	$O(5)$ a5	73.7
D6	DALES	100	e	$O(5)$ a2	73.7, nocorr
D7	DALES	50	e	$O(2)$ a2	46.4
M1	MicroHH	200	SL	$O(2)$ a2	117
M2	MicroHH	100	SL	$O(2)$ a2	73.7
M3	MicroHH	50	SL	$O(2)$ a2	46.4

scheme is rather diffusive, consequently dampens the (co)variance contained in the smallest, resolved scales of the simulations we run (Heinze et al., 2015), and has an effective resolution commensurate with the five grid-point stencil it requires (Bryan et al., 2003). These properties have significant consequences.

Finally, we test the effects of the stability correction on λ by running a single simulation where it is turned off.

We focus our analysis of the simulations on the period before their characteristic moisture length scales approach the domain size, as we wish to eliminate the finite-domain constraints posed by our doubly-periodic boundary conditions.

3 Conceptual model for self-aggregation

We will study the numerical sensitivity of the shallow convective self-aggregation using the conceptual model described by Janssens et al. (2022), which is a closed-form version of the theory introduced by Bretherton and Blossey (2017). The model is briefly summarised in this section; readers looking for a full derivation are encouraged to explore the above manuscripts.

3.1 Definitions

In the following, self-aggregation of the convection in our simulations will be interpreted as growth in mesoscale fluctuations of vertically integrated moisture. To make this more precise, let us define mesoscale fluctuations in a generic scalar χ by partitioning it into its slab-average $\overline{\chi}$ and remaining fluctuation χ', before scale-separating χ' into a mesoscale component χ'_m and sub-mesoscale component χ'_s:

$$\chi = \overline{\chi} + \chi' = \overline{\chi} + \chi'_m + \chi'_s. \tag{10}$$

χ'_m is defined with a spectral low-pass filter at 12.5 km, i.e. fluctuations larger than this scale are considered mesoscale fluctuations.

In our framework, self-aggregation is associated with the development of coherent, mesoscale moist, convecting regions, where $q'_{t_m} > 0$, and dry, non-convecting regions, where $q'_{t_m} < 0$. To identify these regions in our simulations, we use the density-weighted vertical average

$$\langle \chi \rangle = \frac{\int_0^{z_\infty} \rho_0 \chi dz}{\int_0^{z_\infty} \rho_0 dz}, \tag{11}$$

where $z_\infty = 10$ km, yielding the column-averaged, or bulk, moisture $\langle q_t \rangle$. Moist (dry), mesoscale regions as positions where $\langle q'_{t_m} \rangle > 0$ ($\langle q'_{t_m} \rangle < 0$).

With these definitions, we formulate a budget for χ'_m by subtracting the slab-average of eq. 3 from itself, mesoscale-filtering the result, and rewriting several terms:

$$\frac{\partial \chi'_m}{\partial t} = \underbrace{-w'_m \Gamma_\chi}_{\text{Grad. prod.}} \underbrace{-\frac{\partial}{\partial x_{j_h}} \left(u_{j_h} \chi'\right)_m}_{\text{Horizontal transport}} \underbrace{-\frac{1}{\rho_0} \frac{\partial}{\partial z} \left(\rho_0 F_{\chi'_m}\right)}_{\text{Vertical transport}} \underbrace{-\overline{w_{ls}} \frac{\partial \chi'_m}{\partial z}}_{\text{Subsidence}} \underbrace{+\frac{\partial}{\partial x_j} \left(R_{u_j, \chi'_m}\right)}_{\text{SFS diffusion}} \underbrace{+S'_{\chi_m}}_{\text{Source}} \tag{12}$$

In this relation, the slab-averaged vertical gradient $\partial \overline{\chi} / \partial z = \Gamma_\chi$, while $F_{\chi'_m}$ is the anomalous mesoscale vertical flux of χ' around the slab average

$$F_{\chi'_m} = \left(w' \chi'\right)_m - \overline{w' \chi'}. \tag{13}$$

The conceptual model requires eq. 12 to be posed for measures of moisture and heat. To remain consistent with Bretherton and Blossey (2017); Janssens et al. (2022), we will use q_t as our moisture variable, and liquid-water virtual potential temperature, defined as

$$\theta_{lv} = \theta_l + 0.608 \overline{\theta_l} q_t \equiv \theta_v - 7 \overline{\theta_l} q_l, \tag{14}$$

as our heat variable (e.g. B. Stevens, 2007). Both q_t and θ_{lv} are conserved under non-precipitating shallow cumulus convection. Hence, in the absence of radiative heterogeneity, we immediately recognise that $S'_{\chi_m} = 0$. In the following, we will additionally assume that the direct effects of horizontal transport, subsidence and SFS diffusion on the χ'_m budget are small.

3.2 Model

The main features of the conceptual model are captured by fig. 1. Its central panel shows a vertical cross-section of simulation D1 after 16 hours of simulation time, coloured by q_t. Clouds are drawn on top of the q_t field as small, black contour lines. They form preferentially on an anomalously moist, mesoscale patch in the cloud layer (smooth, black contour line, delineating the boundary where $q'_{t_m} = 0$); convection and clouds have self-aggregated into mesoscale structures in this panel.

To explain why, we begin at fig. 1 a), which shows a progressing contrast in q'_{t_m} between moist (blue) and dry (red) regions near the inversion base. Upon vertically averaging eq. 12, it can be shown that the resulting increase in $\langle q'_{t_m} \rangle$ is due primarily to the "gradient production" term, i.e.

$$\frac{\partial \langle q'_{t_m} \rangle}{\partial t} \approx -\langle w'_m \Gamma_{q_t} \rangle \tag{15}$$

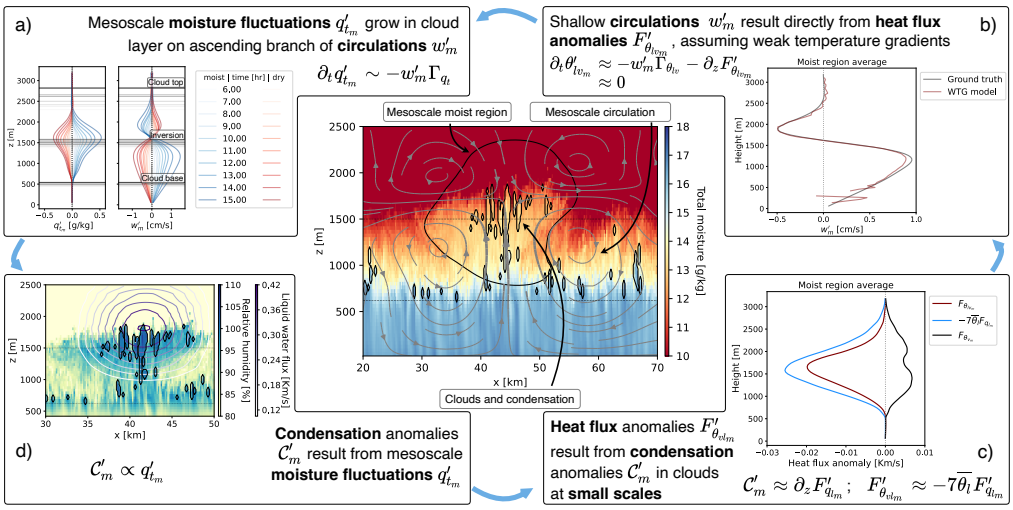

Figure 1. Overview over the circulation-driven self-aggregation mechanism in simulation D1 after 16 hours. Central panel: Example x-z cross-section depicting clouds (small, jagged black contours), which form favourably on a moist, mesoscale region (coloured contours; large, smooth, black contour), in turn driven by a mesoscale circulation (streamlines). Horizontal lines indicate the cloud and inversion bases. a) Vertical profiles of q'_{t_m} and w'_m, averaged over moist (blue) and dry (red) regions, evolving in time (increasing opacity). b) WTG approximation eq. 17 (maroon) of w'_m compared to LES-diagnosed ground-truth (black). c) Mesoscale heat flux anomaly $F'_{\theta_{lvm}}$ (maroon, using eq. 13) and its liquid water flux approximation (blue, using eq. 20). d) As in central panel, but coloured by relative humidity and overlaid by contours of $7\overline{\theta_l}\,(w'q'_l)_m$.

This term expresses transport along the mean, negative moisture gradient with mesoscale vertical velocity anomalies w'_m, which in fig. 1 a) grow increasingly positive (negative) in the moist (dry), cloud layer. w'_m embodies the ascending and descending branches of a shallow circulation (drawn as in-plane streamlines in the central panel of fig. 1), which converges in the moist regions' subcloud layer, transports mixed-layer moisture into the corresponding, moist cloud layer, and diverges near the trade-inversion base into dry regions, where it subsides.

The shallow circulations (w'_m) may be understood as a direct result from heat flux differences between moist and dry mesoscale regions. To show this, consider fig. 1 b). It plots w'_m, averaged over the moist, mesoscale region as i) diagnosed by the LES model, and ii) as predicted by reducing eq. 12 for θ_{lv} to a diagnostic relation:

$$\frac{\partial \theta'_{lv_m}}{\partial t} \approx -w'_m \Gamma_{\theta_{lv}} - \frac{1}{\rho_0}\frac{\partial}{\partial z}\left(\rho_0 F'_{\theta_{lv}m}\right) \approx 0 \tag{16}$$

$$w'_m \approx -\frac{1}{\rho_0}\frac{\partial}{\partial z}\left(\rho_0 F'_{\theta_{lv}m}\right)/\Gamma_{\theta_{lv}}. \tag{17}$$

Eq. 17 essentially amounts to posing the Weak Temperature Gradient (WTG) assumption (e.g. Held & Hoskins, 1985; Sobel et al., 2001), as often successfully employed in models of self-aggregating deep convection (e.g. Emanuel et al., 2014; Chikira, 2014; Beucler et al., 2018; Ahmed & Neelin, 2019). Fig. 1 b) justifies making this assumption for our shallow convective self-aggregation too. Combining eqs. 15 and 17, integrating by parts and ignoring surface flux feedbacks (which are zero by definition in our configuration with homogeneous surface fluxes) then yields a model for $\langle q'_{t_m}\rangle$ which finds its energetic support solely in the heat flux anomaly $F'_{\theta_{lv}m}$, appropriately scaled by the vertical structure of the slab-averaged, thermodynamic state:

$$\frac{\partial \langle q'_{t_m}\rangle}{\partial t} \approx -\left\langle F'_{\theta_{lv}m}\frac{\partial}{\partial z}\left(\frac{\Gamma_{q_t}}{\Gamma_{\theta_{lv}}}\right)\right\rangle \tag{18}$$

To discover why $F'_{\theta_{lv}m}$ develops, let us multiply eq. 14 by w', which decomposes the heat fluxes into flux measures of buoyancy and liquid water:

$$w'\theta'_{lv} \equiv w'\theta'_v - 7\overline{\theta_l}w'q'_l. \tag{19}$$

Fig. 1 c) attributes the primary contribution in this decomposition to liquid water flux anomalies, i.e.

$$F'_{\theta_{lv}m} \approx -7\overline{\theta_l}F'_{q_l m}. \tag{20}$$

In turn, the divergence of $F'_{q_l m}$ stems directly from mesoscale anomalies in the condensation $\mathcal{C}'_m$. Put differently, latent heating in clouds underpins the mesoscale circulation.

Finally, as indicated in fig. 1 d), convective plumes rising into a cloud layer that is moister than the slab mean will condense and later reevaporate more water vapour than average, closing a feedback loop in q'_{t_m}. We express this feedback mathematically by assuming $F'_{q_l m}$ can be written in terms of q'_{t_m} through a poor-man's mass flux approximation:

$$F'_{q_l m} \approx C'w^*q'_{l_m} \approx Cw^*q'_{t_m} \tag{21}$$

In combination, eqs. 18, 20 and 21 give a linear instability model for the moisture-convection feedback with time scale $\tau_{q'_{t_m}}$:

$$\frac{\partial \langle q'_{t_m} \rangle}{\partial t} \approx \frac{\langle q_{t'_m} \rangle}{\tau_{q'_{t_m}}}, \tag{22}$$

$$\tau_{q'_{t_m}} = \frac{1}{C\overline{\theta_l} w^* \frac{\partial}{\partial z}\left(\frac{\Gamma_{q_t}}{\Gamma_{\theta_{lv}}}\right)}. \tag{23}$$

This minimal model is rather accurate for describing the evolution of $\langle q'_{t_m} \rangle$ in simulation D1 (Janssens et al., 2022), and suffices to illustrate how the mechanism is sensitive to discretisation and modelling error.

4 Dependence on sub-mesoscale dynamics

If all assumptions made in deriving eq. 23 hold, it relies on only two variables: A convective velocity scale w^* and the gradient of the ratio of slab averaged lapse rates of heat and moisture, i.e. the vertical structure of the mean environment. Janssens et al. (2022) show that the development of $\partial/\partial z\,(\Gamma_{q_t}/\Gamma_{\theta_{lv}})$ relies only on slab-averaged heat and moisture fluxes; so does $w^*\langle q'_{t_m} \rangle$ through eqs. 20 and 21. Therefore, we pause for a moment to analyse which scales of motion control these fluxes.

Eq. 20 argues that $F'_{\theta_{lv\,m}}$ is facilitated by cumulus clouds, whose energetic scales follow the depth of the boundary layer, of $O(1000)$ m. Hence, the fluctuations in vertical velocity, heat and liquid water that construct $F_{q'_{l_m}}$ and $F_{\theta'_{lv\,m}}$ generally are of a scale much smaller than q'_{t_m}, which by definition is larger than 12.5 km. It is therefore not trivial that $F_{\theta'_{lv\,m}}$ should be controlled by q'_{t_m} as directly as eqs. 20 and 21 suggest.

To illustrate this, consider fig. 2, which shows how the saturation excess $q_t - q_s$ varies over a vertical cross-section of our domain (q_s is the specific humidity at saturation). The white-to-blue contour lines identify a moist, mesoscale patch, with q'_{t_m} up to 0.003 kg/kg near the inversion base at 1500m, which coincides with a region of high $q_t - q_s$, and upon which most of the clouds at these levels consequently form. However, the structure of these clouds, indicated by black contour lines, still varies horizontally with *small* fluctuations in $q_t - q_s$, on a scale commensurate with the cumulus convection itself. As a result, $F_{q'_l}$, $F_{\theta'_{lv}}$ and their mesoscale-filtered counterparts $F_{q'_{l_m}}$ and $F_{\theta'_{lv\,m}}$, plotted over the dashed line at 1500m in the top panel, also remain dominated by sub-mesoscale variation in heat, moisture and vertical velocity. Hence, one might view the mesoscale moisture fluctuations as preconditioners that raise the relative humidity over large regions of the local cumulus layer, while the resulting condensation and diabatic heating in that layer remains governed by sub-mesoscale, cloudy updrafts that carry sub-mesoscale fluctuations of water vapour (q'_{t_s}) into it.

As a result, almost the entire basis of our mesoscale circulation is found in projections of *sub*-mesoscale scalar fluxes onto the mesoscale. More formally, for $\chi' \in \{q'_t, \theta'_{lv}, q'_l\}$, one can scale-decompose a mesoscale-filtered vertical scalar flux as

$$(w'\chi')_m = (w'_m\chi'_m)_m + (w'_m\chi'_s)_m + (w'_s\chi'_m)_m + (w'_s\chi'_s)_m \tag{24}$$

and write the approximation

$$(w'\chi')_m \approx (w'_s\chi'_s)_m \tag{25}$$

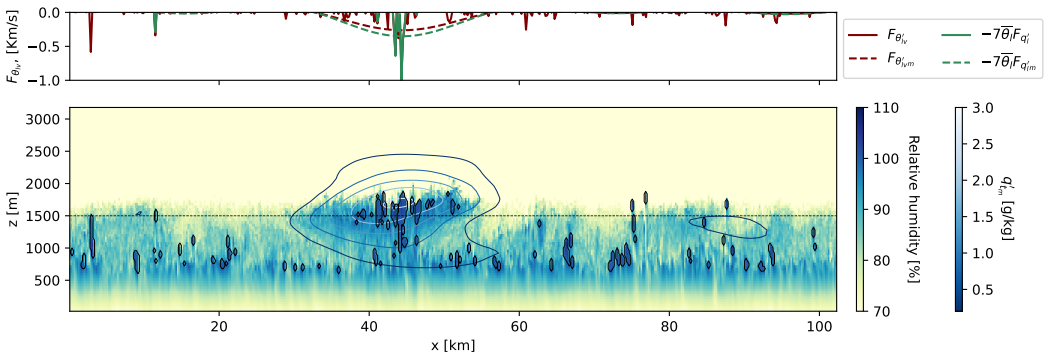

Figure 2. Bottom: Cross-section over the same x-z plane as the extraction plotted in the central panel of fig. 1, coloured by filled contours of relative humidity (yellow to blue) and overlaid by contour lines of i) q'_{t_m} (blue to white lines) and ii) clouds (black lines). Top: Spatial variation of $F_{\theta'_{lv}}$, its mesoscale-filtered counterpart $F_{\theta'_{lv\,m}}$, and their respective liquid-water contributions $-7\overline{\theta_l}F_{q'_l}$ and $-7\overline{\theta_l}F_{q'_{l\,m}}$, over the dashed line at inversion base.

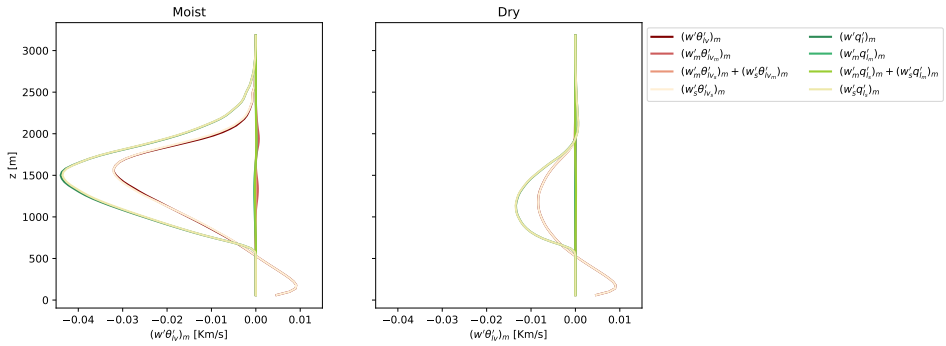

Figure 3. Grid-resolved $(w'\chi')_m$, for $\chi \in \{\theta_{lv}, q_l\}$, ($q_l$ fluxes are scaled by $-7\overline{\theta_l}$), scale-decomposed into pure mesoscale contributions $(w'_m\chi'_m)_m$, cross-scale contributions $(w'_m\chi'_s)_m + (w'_s\chi'_m)_m$ and pure sub-mesoscale contributions $(w'_s\chi'_s)_m$, averaged over 14-16 hours in simulation D1, in moist (left) and dry (right) regions.

to very good accuracy, as shown for both $(w'\theta'_{lv})_m$ and $(w'q'_l)_m$ in fig. 3. Hence, for eq. 23 to successfully explain the evolution of mesoscale moisture anomalies, it is crucial to get the sub-mesoscale fluctuations of w, θ_{lv} and q_l that form them right.

5 Sensitivity to resolution

At $\Delta x = 200$ m, our coarsest simulations barely resolve the energy containing scales of the shallow convection. While the impact of such assumptions may be limited in short simulations on small domains (Siebesma et al., 2003; Blossey et al., 2013), one might imagine simulations of mesoscale structures on large domains, at coarse resolutions and over long integration times to be more sensitive.

Fig. 4 presents the time evolution of vertically integrated mesoscale moisture fluctuations, $\langle q'_{t_m} \rangle$ and the timescale $\tau_{q'_{t_m}}$ estimated from eq. 22 for the numerical model configurations in tab. 1. It shows that repeated grid refinement in the horizontal dimension more than doubles $\tau_{q'_{t_m}}$ in DALES, and quadruples it in MicroHH. The models do not

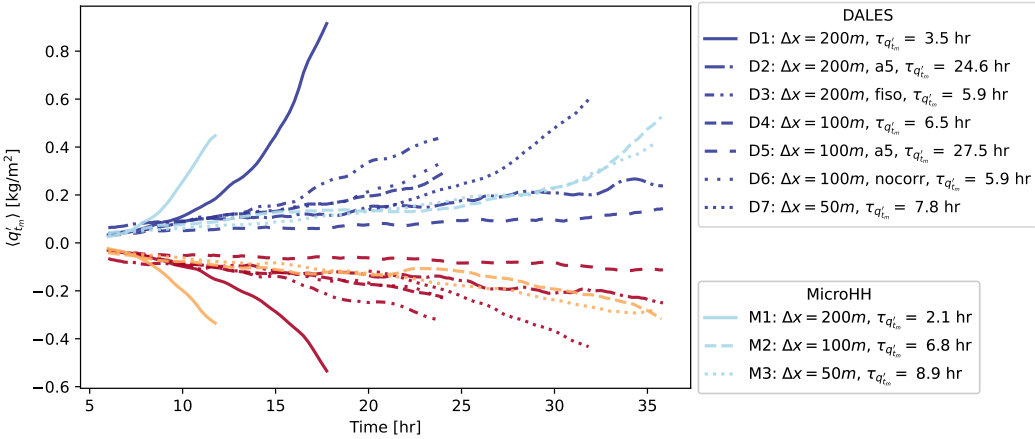

Figure 4. Time-evolution of $\langle q'_{t_m} \rangle$, averaged over moist (blue) and dry (red) mesoscale regions, for numerical configurations indicated by the line styles, in simulations run by DALES (dark colours) and MicroHH (light colours). Abbreviations "fiso", "a5" and "nocorr" follow the definitions from tab. 1.

agree even at $\Delta x = 50$ m. Similar results are obtained for numerical setups that dissipate resolved fluctuations more strongly (simulations D2, D3 and D5). In fact, switching from a second-order advection scheme to a fifth-order scheme (simulations D2 vs. D1 and D5 vs. D4) slows the growth of $\langle q'_{t_m} \rangle$ to the point that it is barely perceptible. In all numerical configurations, the scale growth mechanism eq. 18 holds almost exactly (see fig. S1). Hence, while the form of the circulation-driven mechanism is rather resolution-invariant, its ingredients, w^* and $\Gamma_{q_t}/\Gamma_{\theta_{lv}}$, are not.

To investigate this in more detail, we will focus on how the DALES simulations running at $\Delta x = 200$ m (D1 and D3) and with fifth order advection (D5) and no stability correction (D6) differ from that running at $\Delta x = 100$ m (D4). Since our length scale growth model is state-dependent, such differences are best studied by tracing the temporal divergence between experiments that start from an identical state after the model spinup. We choose that state to be simulation D4's solution after 12 hours, when mesoscale fluctuations are small. For simulations D1 and D3, this solution is first coarse-grained onto a grid with $\Delta x = 200$ m using a top-hat filter. We then run the cases on for 12 hours with all other settings kept identical to simulations D1, D3, D5 and D6.

Fig. 5 shows how profiles of the ingredients to eq. 18 evolve in these simulations in the first six hours after they have been relaunched. Their q'_{t_m} fields are initially identical, as is $\Gamma_{q_t}/\Gamma_{\theta_{lv}}$. However, this state immediately elicits a response in the coarser simulations' $F_{\theta'_{lv_m}}$. It increase in strength, amplifying $w'_m \Gamma_{q_t}$. As a result, q'_{t_m} begins growing more quickly in these simulations, supplying additional fuel that $F_{\theta'_{lv_m}}$ can feed on; the mechanism and divergence between the simulations intensifies over time.

It is worth noting that the main sinks in the q'_{t_m} and θ'_{lv_m} budgets, the horizontal advection terms, barely respond to the changes in grid spacing (see fig. S1 and S2). The faster growth of q'_{t_m} in our coarse simulations is then not because mesoscale fluctuations are horizontally redistributed or dissipated down to the sub-mesoscale less efficiently, but due to an enhancement of $F_{\theta'_{lv_m}}$-driven production at a given q'_{t_m}. Put differently, it is the proportionality in eqs. 20 and 21 that is not grid-converged.

Why is the development of $F_{\theta'_{lv_m}}$ resolution-sensitive? The spectra plotted in fig. 6 offer a suggestion. In the first hour after the coarse-resolution simulation D1 has been

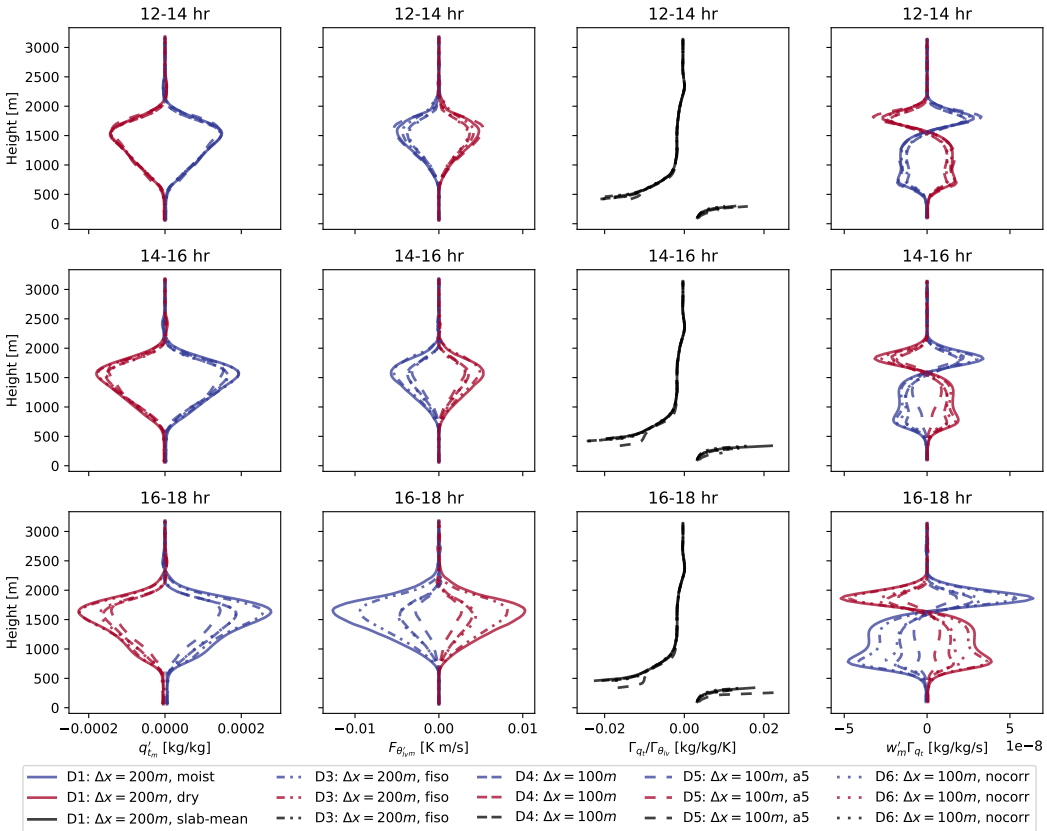

Figure 5. Vertical profiles of q'_{t_m}, $F_{\theta'_{lv\,m}}$, $\Gamma_{q_t}/\Gamma_{\theta_{lv}}$ and $w'_m\Gamma_{q_t}$ (columns left to right), in moist and dry regions (blue and red lines), averaged over 2-hour intervals (top to bottom rows) after launching the cases D1, D3, D5 and D6 from the case D4 (different line styles).

relaunched from the finer-resolution simulation D4, it contains slightly less variance in its smallest scales of q_t, w and θ_{lv} in the sub-cloud layer (figs. 6 a-c). But in the cloud layer, where our instability resides, fluctuations in q_t, w and θ_{lv} are more energetic at their smallest, resolved scales (figs. 6 d-f) in simulation D1 than in D4. At the inversion base, where $F_{\theta'_{lv\,m}}$ reaches its maximum, the small-scale fluctuations in the coarse simulation are more energetic still (figs. 6 g-i).

The excess variance in inversion-layer q_t is initially almost ephemeral: Fig. 6 g) shows that the inversion-layer moisture field is dominated by its largest scales (wavenumbers smaller than k_m), which remain unaffected by the restart. In contrast, the variance in both w and θ_{lv} peaks at wavenumbers commensurate with the boundary layer height of $O(1000)$ m, and retains a non-negligible contribution from a long range of scales smaller than that, especially in the cloud and inversion layers. In our coarse simulations, it is the excess small-scale w' and θ'_{lv} in these two layers that through eq. 25 provide the variance that underpins the stronger $F_{\theta'_{lv\,m}}$ and subsequent development of q'_{t_m}.

The spectral variance plateau at the smallest, resolved scales at $z = 1500$ m persists even when $\Delta x = 100$ m, explaining why simulations D7 and M3 ($\Delta x = 50$ m) self-aggregate over an even longer time scale than simulations D4 and M2 ($\Delta x = 100$ m). In fact, the plateau even persists in the inversion layer at $\Delta x = 50$ m (see fig. S3), raising questions as to whether the self-aggregation even in those simulations would be

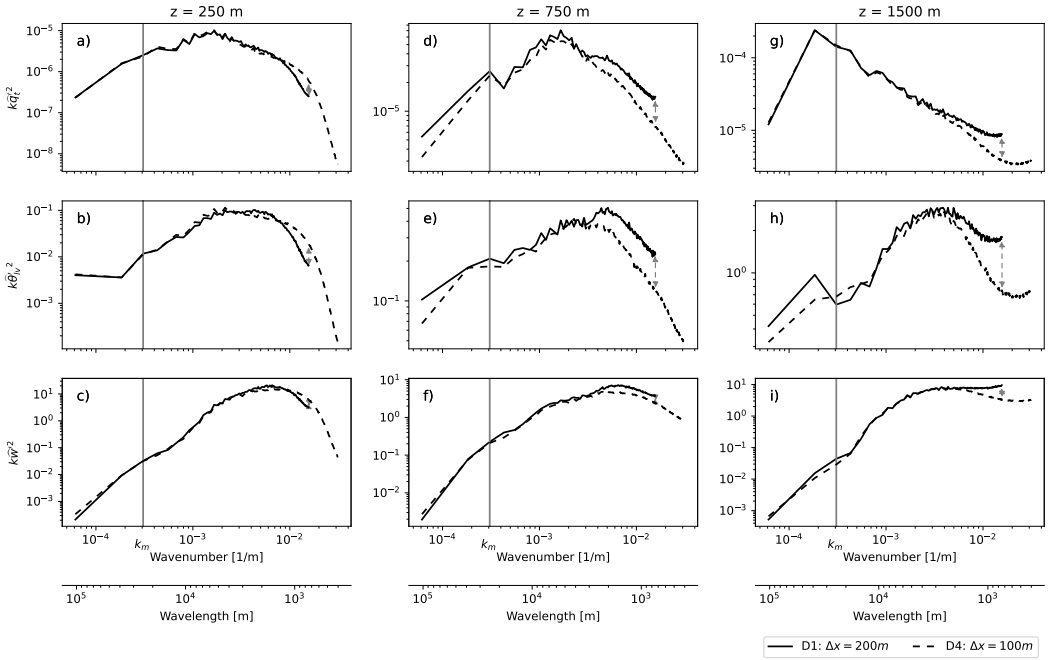

Figure 6. Radial power spectral density of q_t ($k\widehat{q_t'}^2$, a, d, g) θ_{lv} ($k\widehat{\theta_{lv}'}^2$, b, e, h) and w ($k\widehat{w'}^2$, c, f, i) for our 100m simulation (D4) and 200m simulation (D1) restarted from D4, averaged over the first hour after the restart, over x-y cross-sections at 250m (a-c, in middle of sub-cloud layer), 750m (d-f, in cloud layer) and 1500m (g-i, at inversion base). k_m indicates the wavenumber that separates the mesoscales from the sub-mesoscales, according to eq. 10.

grid-independent. Simulations with stronger diffusion (D3, D5 nad D6, see fig. S4) dampen the spectral plateau, and consequently reduce $F_{\theta'_{lvm}}$ compared to simulation D1 (see fig. 5).

So which, if any, of the results above can we trust? It is impossible to answer this question completely in the absence of observations. However, we believe we may eliminate some ambiguity by testing the degree to which the simulations hold up to the fundamental LES assumption that our quantities of interest should be independent of SFS effects. The SFS models employed in DALES and MicroHH assume these effects can reasonably be modelled by diffusion with diffusivity $K_m \sim u''l''$, where u'' and l'' are typical velocity and length scales of the unresolved motions in the flow. This approximation can be rationalised if $l'' \sim \Delta$ resides in the inertial subrange of homogeneous, isotropic turbulence. In the inertial subrange, the mean rate of transfer of turbulent kinetic energy e from any scale to a smaller one is scale-independent, and equal to the rate at which it is eventually dissipated by molecular diffusion at much smaller scales, ε (e.g. Wyngaard, 2010). Therefore, we are satisfied with resolving the larger, energy-containing eddies, characterised by velocity and length scales U and L, respectively, inserting Δ in the inertial subrange, and employing a diffusive SFS model that we only ask to model ε correctly. If it does, a necessary requirement is that ε is independent of Δ, and thus of our grid spacing (Sullivan & Patton, 2011). Fig. 7 shows that this is not the case; our coarse-mesh simulations underestimate ε with respect to our fine-mesh simulations throughout the cloud layer, and this underdissipation accelerates the observed length scale growth (fig. S5 paints the same picture for our MicroHH simulations). We are either making mistakes within our model for ε at $\Delta x \in [100, 200]$ m, or must concede that these grid spacings are simply too coarse to reside in the inertial subrange.

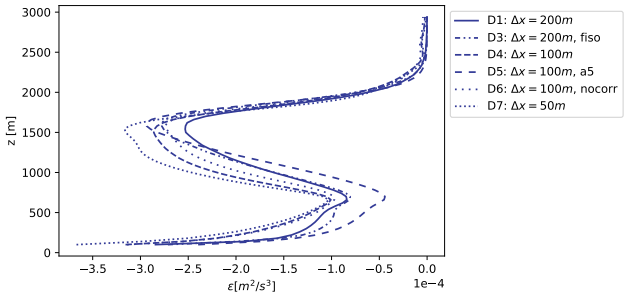

Figure 7. Profiles of dissipation ε of resolved turbulent kinetic energy e, averaged between 12-14 hr, for numerical configurations indicated by the line styles, in simulations run by DALES.

Several pieces of evidence assign a high likelihood to the second of these options holding some truth. First, let us attempt to account for our anisotropic grid, which makes us underestimate Δ in the horizontal direction. It is in principle possible that the insufficient dissipation we observe stems from our abuse of this length scale. However, setting $\Delta = \Delta x$ according to Deardorff (1980)'s original proposition (simulation D3) still underestimates the dissipation with respect to higher-resolution simulations, even though it strongly overestimates the vertical component of this length scale relative to the vertical grid spacing. It is thus unlikely that our grid anisotropy alone is responsible for underestimating ε. Second, our empirical stability corrections might over-ambitiously diminish the eddy diffusivities in stratified regions. This too could explain the excess small-scale variance, as it rises as the stratification increases through the cloud and inversion layers. Yet, switching off the stability correction entirely (simulation D6) only slightly reduces the small-scale variance, and does not measurably influence the evolution. Therefore, it is also unlikely that stability corrections are at the root of the problem. Third, the underestimation of dissipation is consistent across two independent LES codes with different thermodynamics and SFS models, and is thus unlikely related to individual model details. Finally, we remark that our resolutions may simply be too low to allow a proper turbulent flow to develop on the resolved scales. If we had such a flow, its large-eddy Reynolds number $\mathrm{Re}_L \gg 1$. Following Wyngaard (1984),

$$\mathrm{Re}_L = \frac{UL}{K_m} \sim \frac{UL}{u''\Delta} \sim \frac{UL}{\varepsilon^{\frac{1}{3}}\Delta^{\frac{4}{3}}} \sim \left(\frac{L}{\Delta}\right)^{\frac{4}{3}}, \tag{26}$$

if $\varepsilon \sim U^3/L \sim u''^3/\Delta$, which holds if Δ resides in the inertial subrange (Tennekes & Lumley, 1972). In our simulations, $L \sim 1000$ m, and we attain $\mathrm{Re}_L \sim 10$ for $\Delta x \in [100, 200]$ m; this number is even lower for simulations with the $O(5)$ advection scheme, whose effective resolution is approximately $6\Delta x$ (Bryan et al., 2003). Simulations of organised, deep convection indicate that $\mathrm{Re}_L \sim 10^2$ may be necessary for the flow to enter a regime where its statistics no longer scale with Re_L (Bryan et al., 2003); the same seems necessary for certain shallow cumulus cases (D. E. Stevens et al., 2002). Thus, grid spacings at the lower end of what we test here, or even finer, may be required to simulate organising shallow cumulus in LES, and any subsequent transition to deep, organised convection, unless SFS models are employed that do not rely on Δ residing in the inertial subrange.

6 Discussion

We find that the numerical representation of fluctuations in buoyancy and vertical velocity in shallow cumuli at scales smaller than 1 km have the potential to propa-

gate into significant differences in the moisture field at scales up to the 100 km domain sizes simulated here. We draw attention to a few implications for the modelling of tropical convection.

First, it is worthwhile to place these results in the context of early LES model intercomparisons. In the BOMEX intercomparison (Siebesma et al., 2003), small-domain LES models agreed well with each other at the resolutions considered here. It proved much harder to achieve similar agreement for shallow cumulus under strong inversions, such as those that develop in conditions sampled during the Atlantic Tradewind Experiment (ATEX) (B. Stevens et al., 2001). It is precisely in the inversion, where the energy-containing turbulent length scales shrink below the boundary layer's depth (e.g. Mellado et al., 2014, 2017), that we find both the key to circulation-driven self-aggregation, and our SFS models lacking. Given the tight coupling between the fluxes that grow the cumulus layer (B. Stevens, 2007) and those that lead to its self-aggregation (Janssens et al., 2022), we wonder whether our results simply give the historical context of the ATEX intercomparison a new perspective: It is perhaps simply too ambitious to simulate large-scale cloud structures that depend so strongly on inversion-layer dynamics at resolutions tractable for large-eddy simulations.

In particular, our results suggest why the structures termed "flowers" by B. Stevens et al. (2020) are inadequately captured in simulations of even coarser resolution than considered here (Schulz, 2021): They may just run an overly dissipative combination of advection scheme and unresolved scales model. The results also indicate that small-scales driven development of mesoscale scalar variance poses a fitting and challenging test case for the development of better parameterisations in the convective gray zone, such as those discussed in (Honnert et al., 2020), and ultimately to the development of the next generation of cumulus parameterisations in global models, which are unable to adequately estimate the contribution from the trades towards the equilibrium climate sensitivity (Myers et al., 2021; Cesana & Del Genio, 2021). At minimum, our results suggest that it is prudent for modelling studies of the spontaneous development of mesoscale shallow cloud patterns to incorporate an assessment of their degree of grid convergence. Concretely, we recommend to always assess the resolution sensitivity of one's quantities of interest, e.g. $\langle q'_{t_m} \rangle$, and of our indicators of mesoscale variance production, e.g. $F'_{\theta_{lvm}}$ or $\tau_{q'_{t_m}}$. If such sensitivities are found, inversion-layer w or heat spectra may offer insight into the sensitivity's origins.

We pose our recommendations on the basis of simulations with minimal physics. Therefore, it may not be immediately obvious why our results should be of interest to situations where radiation, precipitation or strong boundary forcings prevail over the moist convection. Yet, simulations of such situations often first appear to require non-precipitating cumulus to aggregate sufficient amounts of moisture into moist mesoscale regions before developing stratiform cloud layers and cold pools (Bretherton & Blossey, 2017; Narenpitak et al., 2021), which may then modulate the mesoscale dynamics (Vogel et al., 2016; Anurose et al., 2020). Additionally, the microphysical parameterisations upon which such precipitation-driven mechanisms rely typically exhibit even larger model biases than the turbulence-parameterisations discsussed here (e.g. van Zanten et al., 2011). If such parameterisations are not even driven by the right model dynamics, they can also not be expected to return realistic precipitation and cold pools. Exactly how large error propagation from dynamics-to-physics modules is for self-organising cumulus convection remains largely unquantified; appraising and amending such estimates is therefore a worthwhile topic of future research.

Finally, we return to the matter of self-aggregation in simulations of radiative-convective equilibrium discussed in the introduction. Our coarsest two simulations (D1 and M1) develop deep convective clouds on top of their mesoscale moist regions, displaying some form of radiation- and precipitation-less, deep convective self-aggregation. We do not argue that these clouds are physical. Yet, their development does open a potential path

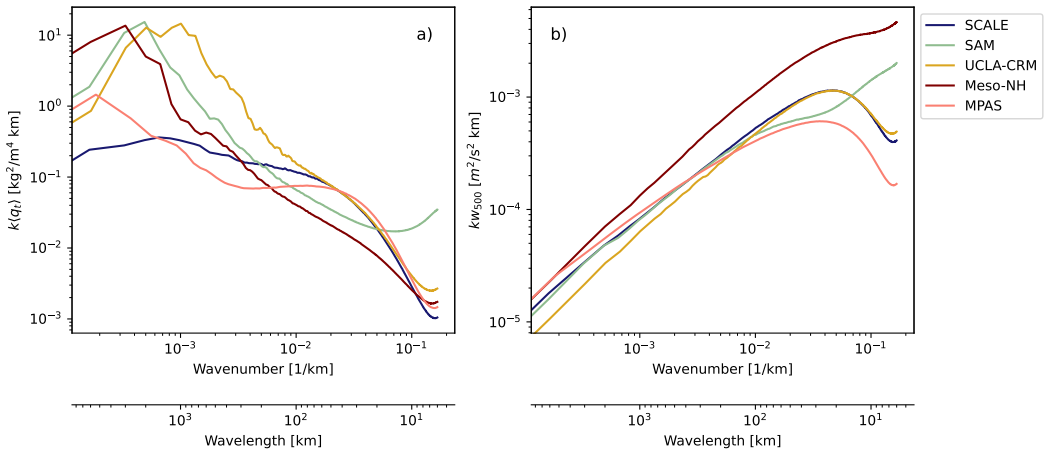

Figure 8. Power-spectral densities of $\langle q_t \rangle$ (a) and w_{500} (vertical velocity at 500 hPa, b) of five participating models in the RCE Model Intercomparison Project (RCEMIP), in the RCE-large configuration detailed by Wing et al. (2018), over a sea surface at 300K and averaged over the last 50 days of simulation. Simulations with more energetic small-scale vertical velocity fluctuations contain more variance in their largest scales of moisture.

between the convective feedback in the shallow convection discussed here and the shallow circulations that underlie deep convective self-aggregation. Therefore, our results may contribute to explain why numerical models set up on the same numerical domain, but with different advection schemes and SFS models, self-aggregate so differently in RCE (Wing et al., 2020). Running with grid spacings exceeding 1 km - i.e. a factor five greater than the coarsest grids used here - these simulations may simply dissipate energy from their oft-parameterised shallow convection at different rates and thus support highly variable circulation strengths and self-aggregation time scales (Shamekh et al., 2020). The spectra of vertically integrated water vapour and vertical velocity of several simulations that participate in Wing et al. (2020) bear these hallmarks (fig. 8). More study of choices in discretisation and unresolved scales schemes, and the resulting interaction of numerical and modelling errors with the resolved dynamics in cloud-resolving models of RCE is warranted.

7 Summary

In pursuit of understanding why and when idealised models of tropical convection self-aggregate, we have studied the sensitivity to numerical settings of self-aggregating shallow cumulus convection. In idealised large-eddy simulations with a homogeneous surface forcing and no radiation or precipitation models, spontaneous aggregation is facilitated by a pure, convective instability: Small fluctuations in latent heating in shallow cumulus clouds prompt mesoscale circulations which transport moisture from dry to moist columns, resulting in aggregated patches of cumulus clouds which release more latent heat and strengthen the circulations.

The instability represents a pathway for sub-mesoscale, turbulent fluxes of heat and moisture in kilometre-scale cumulus clouds to control the moisture variability at scales up to two orders of magnitude larger. Therefore, modellers must take great care when trying to represent the underlying, turbulent dynamics in LES or cloud-resolving models: We find that the time scale of the instability is highly sensitive to differences in grid spacing and advection scheme, over a range of rather conventional choices for LES mod-

elling of shallow cumulus (fig. 4); even at $\Delta x = 50$ m grid spacings, we find two LES codes with different SFS models to aggregate at rather different time scales. Given the potential role played by shallow convection in developing and maintaining deep convective self-aggregation, we wonder whether similar differences in how cloud-resolving models represent the effects of shallow convection matter in explaining the abundance of aggregation varieties observed in simulations of deep convection in RCE.

Our results call for a thorough analysis of the degree to which models of shallow convective self-aggregation match reality, a question which has remained elusive for studies of their deep-convective counterparts (Muller et al., 2022). A good start in this direction is offered by simulations of the EUREC^{4}A field campaign (Narenpitak et al., 2021; Saffin et al., 2022), which exhibit circulation-driven moisture aggregation in more realistic settings, and which compare favourably to the campaign's observations. In fact, these observations include sufficiently detailed observations of mesoscale circulations (George et al., 2021) that the data required to reconcile models and nature may be in hand, boding well for our understanding of self-aggregating convection.

8 Open Research

Frozen images of the versions of DALES and MicroHH used in this study have been stored at `https://doi.org/10.5281/zenodo.6545655` and `https://doi.org/10.5281/zenodo.822842` respectively. The numerical settings, routines and post-processed simulation data used to generate the figures presented in the manuscript are available at `https://doi.org/10.5281/zenodo.6772483`. Living repositories for DALES, MicroHH and the postprocessing scripts are available at `https://github.com/dalesteam/dales`, `https://github.com/microhh/microhh` and `https://github.com/martinjanssens/ppagg`, respectively. Both DALES and MicroHH are released under the GNU General Public License v3.0. The standardized RCEMIP data is hosted by the German Climate Computing Center (DKRZ) and is publicly available at `https://www.wdc-climate.de/ui/info?site=RCEMIP_DS`.

Acknowledgments

CvH acknowledges funding from the Dutch Research Council (NWO) (grant: VI.Vidi.192.068). A. Pier Siebesma acknowledges funding by the European Union's Horizon 2020 research and innovation program under grant agreement no. 820829 (CONSTRAIN project). FG acknowledges support from The Branco Weiss Fellowship - Society in Science, administered by ETH Zürich, and from an NWO Veni grant. For use of their computational resources, we thank both NWO (project 2021/ENW/01081379) and RIKEN (project hp200321 of the HPCI System Research Project for access to the Fugaku supercomputer).

References

Ahmed, F., & Neelin, J. D. (2019). Explaining scales and statistics of tropical precipitation clusters with a stochastic model. *Journal of the Atmospheric Sciences*, *76*(10), 3063–3087.

Anurose, T., Bašták Ďurán, I., Schmidli, J., & Seifert, A. (2020). Understanding the moisture variance in precipitating shallow cumulus convection. *Journal of Geophysical Research: Atmospheres*, *125*(1), e2019JD031178.

Beucler, T., Cronin, T., & Emanuel, K. (2018). A linear response framework for radiative-convective instability. *Journal of Advances in Modeling Earth Systems*, *10*(8), 1924–1951.

Beucler, T., & Cronin, T. W. (2016). Moisture-radiative cooling instability. *Journal of Advances in Modeling Earth Systems*, *8*(4), 1620–1640.

Blossey, P. N., Bretherton, C. S., Zhang, M., Cheng, A., Endo, S., Heus, T., ... Xu,

K.-M. (2013). Marine low cloud sensitivity to an idealized climate change: The cgils les intercomparison. *Journal of Advances in Modeling Earth Systems*, *5*(2), 234–258.

Böing, S. (2016). An object-based model for convective cold pool dynamics. *Mathematics of Climate and Weather Forecasting*, *2*(1).

Bretherton, C. S., & Blossey, P. N. (2017). Understanding mesoscale aggregation of shallow cumulus convection using large-eddy simulation. *Journal of Advances in Modeling Earth Systems*, *9*(8), 2798–2821.

Bretherton, C. S., Blossey, P. N., & Khairoutdinov, M. (2005). An energy-balance analysis of deep convective self-aggregation above uniform sst. *Journal of the atmospheric sciences*, *62*(12), 4273–4292.

Bryan, G. H., Wyngaard, J. C., & Fritsch, J. M. (2003). Resolution requirements for the simulation of deep moist convection. *Monthly Weather Review*, *131*(10), 2394–2416.

Cesana, G. V., & Del Genio, A. D. (2021). Observational constraint on cloud feedbacks suggests moderate climate sensitivity. *Nature Climate Change*, *11*(3), 213–218.

Chikira, M. (2014). Eastward-propagating intraseasonal oscillation represented by chikira–sugiyama cumulus parameterization. part ii: Understanding moisture variation under weak temperature gradient balance. *Journal of the Atmospheric Sciences*, *71*(2), 615–639.

Deardorff, J. W. (1973). Three-dimensional numerical modeling of the planetary boundary layer. In *Workshop on micrometeorogy, 1973.*

Deardorff, J. W. (1980). Stratocumulus-capped mixed layers derived from a three-dimensional model. *Boundary-layer meteorology*, *18*(4), 495–527.

de Roode, S. R., Siebesma, A. P., Jansson, F., & Janssens, M. (2022). Dependency of mesoscale organization on grid anisotropy in large-eddy simulations. *Under review at Journal of Advances in Modeling Earth Systems (JAMES).*

Emanuel, K., Wing, A. A., & Vincent, E. M. (2014). Radiative-convective instability. *Journal of Advances in Modeling Earth Systems*, *6*(1), 75–90.

George, G., Stevens, B., Bony, S., Pincus, R., Fairall, C., Schulz, H., ... others (2021). Joanne: Joint dropsonde observations of the atmosphere in tropical north atlantic meso-scale environments. *Earth System Science Data*, *13*(11), 5253–5272.

George, G., Stevens, B., Bony, S., Vogel, R., & Naumann, A. K. (2022). *The ubiquity of shallow circulations in the trades* (Tech. Rep.). Copernicus Meetings.

Grabowski, W. W., & Moncrieff, M. (2004). Moisture–convection feedback in the tropics. *Quarterly Journal of the Royal Meteorological Society: A journal of the atmospheric sciences, applied meteorology and physical oceanography*, *130*(604), 3081–3104.

Haerter, J. O. (2019). Convective self-aggregation as a cold pool-driven critical phenomenon. *Geophysical Research Letters*, *46*(7), 4017–4028.

Heinze, R., Mironov, D., & Raasch, S. (2015). Second-moment budgets in cloud topped boundary layers: A large-eddy simulation study. *Journal of Advances in Modeling Earth Systems*, *7*(2), 510–536.

Held, I. M., & Hoskins, B. J. (1985). Large-scale eddies and the general circulation of the troposphere. In *Advances in geophysics* (Vol. 28, pp. 3–31). Elsevier.

Heus, T., van Heerwaarden, C. C., Jonker, H. J., Siebesma, A. P., Axelsen, S., van den Dries, K., ... others (2010). Formulation of and numerical studies with the Dutch Atmospheric Large-Eddy Simulation (DALES). *Geosci. Model Dev*, *3*, 415–444.

Honnert, R., Efstathiou, G. A., Beare, R. J., Ito, J., Lock, A., Neggers, R., ... Zhou, B. (2020). The atmospheric boundary layer and the "gray zone" of turbulence: A critical review. *Journal of Geophysical Research: Atmospheres*, *125*(13), e2019JD030317.

Janssens, M., de Arellano, J. V.-G., van Heerwaarden, C. C., de Roode, S. R., Siebesma, A. P., & Glassmeier, F. (2022). *Non-precipitating shallow cumulus convection is intrinsically unstable to length-scale growth.* arXiv. Retrieved from `https://arxiv.org/abs/2206.14739` doi: 10.48550/ARXIV.2206.14739

Jeevanjee, N., & Romps, D. M. (2013). Convective self-aggregation, cold pools, and domain size. *Geophysical Research Letters*, *40*(5), 994–998.

Klinger, C., Mayer, B., Jakub, F., Zinner, T., Park, S.-B., & Gentine, P. (2017). Effects of 3-d thermal radiation on the development of a shallow cumulus cloud field. *Atmospheric Chemistry and Physics*, *17*(8), 5477–5500.

Kuang, Z. (2018). Linear stability of moist convecting atmospheres. part i: From linear response functions to a simple model and applications to convectively coupled waves. *Journal of the Atmospheric Sciences*, *75*(9), 2889–2907.

Lamaakel, O., & Matheou, G. (2022). Organization development in precipitating shallow cumulus convection: Evolution turbulence characteristics. *Journal of the Atmospheric Sciences*.

Lilly, D. K. (1968). Models of cloud-topped mixed layers under a strong inversion. *Quarterly Journal of the Royal Meteorological Society*, *94*(401), 292–309.

Mellado, J. P., Puche, M., & Van Heerwaarden, C. C. (2017). Moisture statistics in free convective boundary layers growing into linearly stratified atmospheres. *Quarterly Journal of the Royal Meteorological Society*, *143*(707), 2403–2419.

Mellado, J. P., Stevens, B., & Schmidt, H. (2014). Wind shear and buoyancy reversal at the top of stratocumulus. *Journal of the Atmospheric Sciences*, *71*(3), 1040–1057.

Muller, C., & Bony, S. (2015). What favors convective aggregation and why? *Geophysical Research Letters*, *42*(13), 5626–5634.

Muller, C., & Held, I. M. (2012). Detailed investigation of the self-aggregation of convection in cloud-resolving simulations. *Journal of the Atmospheric Sciences*, *69*(8), 2551–2565.

Muller, C., Yang, D., Craig, G., Cronin, T., Fildier, B., Haerter, J. O., ... others (2022). Spontaneous aggregation of convective storms. *Annual Review of Fluid Mechanics*, *54*, 133–157.

Myers, T. A., Scott, R. C., Zelinka, M. D., Klein, S. A., Norris, J. R., & Caldwell, P. M. (2021). Observational constraints on low cloud feedback reduce uncertainty of climate sensitivity. *Nature Climate Change*, *11*(6), 501–507.

Narenpitak, P., Kazil, J., Yamaguchi, T., Quinn, P. K., & Feingold, G. (2021). From sugar to flowers: A transition of shallow cumulus organization during atomic. *Journal of Advances in Modeling Earth Systems*, *13*, e2021MS002619.

Ouwersloot, H., Moene, A., Attema, J., & De Arellano, J. V.-G. (2017). Large-eddy simulation comparison of neutral flow over a canopy: Sensitivities to physical and numerical conditions, and similarity to other representations. *Boundary-Layer Meteorology*, *162*(1), 71–89.

Raymond, D. J., Sessions, S. L., Sobel, A. H., & Fuchs, Ž. (2009). The mechanics of gross moist stability. *Journal of Advances in Modeling Earth Systems*, *1*(3).

Saffin, L., Marsham, J., Blyth, A., & Parker, D. (2022). *Mesoscale organisation transition during the 2nd feb eurec4a case study simulated by a high-resolution weather model* (Tech. Rep.). Copernicus Meetings.

Schulz, H. (2021). *Meso-scale patterns of shallow convection in the trades* (Doctoral dissertation, Universität Hamburg). doi: 10.17617/2.3357904

Seifert, A., & Heus, T. (2013). Large-eddy simulation of organized precipitating trade wind cumulus clouds. *Atmospheric Chemistry and Physics*, *13*(11), 5631–5645.

Seifert, A., Heus, T., Pincus, R., & Stevens, B. (2015). Large-eddy simulation of the transient and near-equilibrium behavior of precipitating shallow convection. *Journal of Advances in Modeling Earth Systems*, *7*(4), 1918–1937.

Shamekh, S., Muller, C., Duvel, J.-P., & d'Andrea, F. (2020). Self-aggregation of convective clouds with interactive sea surface temperature. *Journal of Advances in Modeling Earth Systems*, *12*(11), e2020MS002164.

Siebesma, A. P., Bretherton, C. S., Brown, A., Chlond, A., Cuxart, J., Duynkerke, P. G., ... others (2003). A large eddy simulation intercomparison study of shallow cumulus convection. *Journal of the Atmospheric Sciences*, *60*(10), 1201–1219.

Siebesma, A. P., & Cuijpers, J. W. M. (1995). Evaluation of parametric assumptions for shallow cumulus convection. *Journal of Atmospheric Sciences*, *52*(6), 650–666.

Sobel, A. H., Nilsson, J., & Polvani, L. M. (2001). The weak temperature gradient approximation and balanced tropical moisture waves. *Journal of the atmospheric sciences*, *58*(23), 3650–3665.

Stevens, B. (2007). On the growth of layers of nonprecipitating cumulus convection. *Journal of the atmospheric sciences*, *64*(8), 2916–2931.

Stevens, B., Ackerman, A. S., Albrecht, B. A., Brown, A. R., Chlond, A., Cuxart, J., ... others (2001). Simulations of trade wind cumuli under a strong inversion. *Journal of the Atmospheric Sciences*, *58*(14), 1870–1891.

Stevens, B., Bony, S., Brogniez, H., Hentgen, L., Hohenegger, C., Kiemle, C., ... others (2020). Sugar, gravel, fish and flowers: Mesoscale cloud patterns in the trade winds. *Quarterly Journal of the Royal Meteorological Society*, *146*(726), 141–152.

Stevens, D. E., Ackerman, A. S., & Bretherton, C. S. (2002). Effects of domain size and numerical resolution on the simulation of shallow cumulus convection. *Journal of the atmospheric sciences*, *59*(23), 3285–3301.

Sullivan, P. P., & Patton, E. G. (2011). The effect of mesh resolution on convective boundary layer statistics and structures generated by large-eddy simulation. *Journal of the Atmospheric Sciences*, *68*(10), 2395–2415.

Tennekes, H., & Lumley, J. L. (1972). *A first course in turbulence*. MIT press.

Tompkins, A. M. (2001). On the relationship between tropical convection and sea surface temperature. *Journal of climate*, *14*(5), 633–637.

Tompkins, A. M., & Semie, A. G. (2017). Organization of tropical convection in low vertical wind shears: Role of updraft entrainment. *Journal of Advances in Modeling Earth Systems*, *9*(2), 1046–1068.

Van Heerwaarden, C. C., Van Stratum, B. J., Heus, T., Gibbs, J. A., Fedorovich, E., & Mellado, J. P. (2017). Microhh 1.0: a computational fluid dynamics code for direct numerical simulation and large-eddy simulation of atmospheric boundary layer flows. *Geoscientific Model Development*, *10*(8), 3145–3165.

van Zanten, M. C., Stevens, B., Nuijens, L., Siebesma, A. P., Ackerman, A., Burnet, F., ... others (2011). Controls on precipitation and cloudiness in simulations of trade-wind cumulus as observed during rico. *Journal of Advances in Modeling Earth Systems*, *3*(2).

Vogel, R., Nuijens, L., & Stevens, B. (2016). The role of precipitation and spatial organization in the response of trade-wind clouds to warming. *Journal of Advances in Modeling Earth Systems*, *8*(2), 843–862.

Wicker, L. J., & Skamarock, W. C. (2002). Time-splitting methods for elastic models using forward time schemes. *Monthly weather review*, *130*(8), 2088–2097.

Wing, A. A., Reed, K. A., Satoh, M., Stevens, B., Bony, S., & Ohno, T. (2018). Radiative–convective equilibrium model intercomparison project. *Geoscientific Model Development*, *11*(2), 793–813.

Wing, A. A., Stauffer, C. L., Becker, T., Reed, K. A., Ahn, M.-S., Arnold, N. P., ... others (2020). Clouds and convective self-aggregation in a multimodel ensemble of radiative-convective equilibrium simulations. *Journal of advances in modeling earth systems*, *12*(9), e2020MS002138.

Wyngaard, J. C. (1984). Boundary-layer modeling. In *Atmospheric turbulence and*

air pollution modelling (pp. 69–106). Springer.

Wyngaard, J. C. (2010). *Turbulence in the atmosphere.* Cambridge University Press.

Yang, D. (2021). A shallow-water model for convective self-aggregation. *Journal of the Atmospheric Sciences*, *78*(2), 571–582.

Figure 1.

a)

Mesoscale **moisture fluctuations** q'_{t_m} grow in cloud layer on ascending branch of **circulations** w'_m

$$\partial_t q'_{t_m} \sim -w'_m \Gamma_{q_t}$$

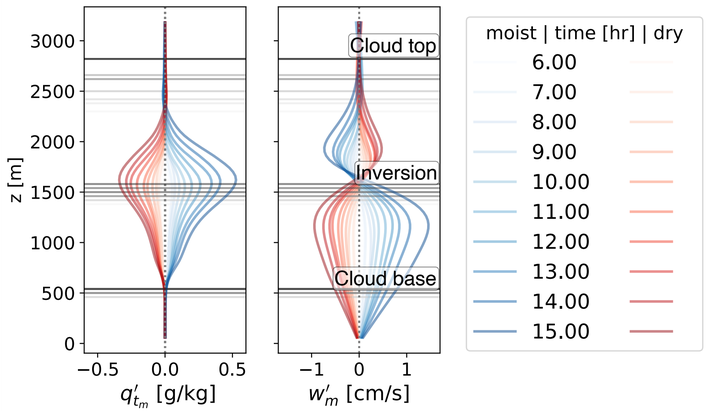

b)

Shallow **circulations** w'_m result directly from **heat flux anomalies** $F'_{\theta_{lv_m}}$, assuming weak temperature gradients

$$\partial_t \theta'_{lv_m} \approx -w'_m \Gamma_{\theta_{lv}} - \partial_z F'_{\theta_{lv_m}} \approx 0$$

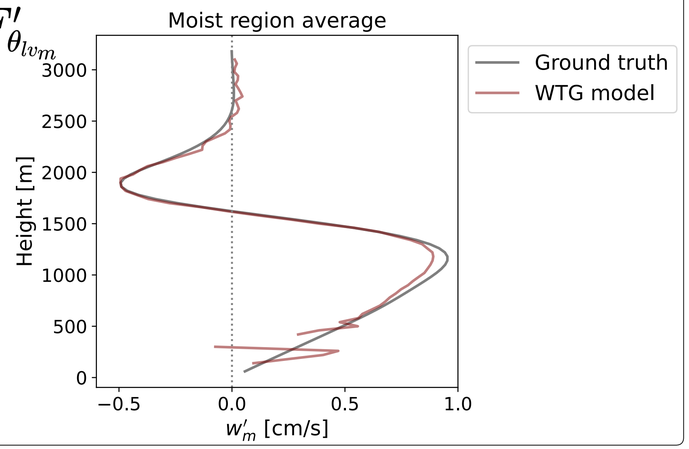

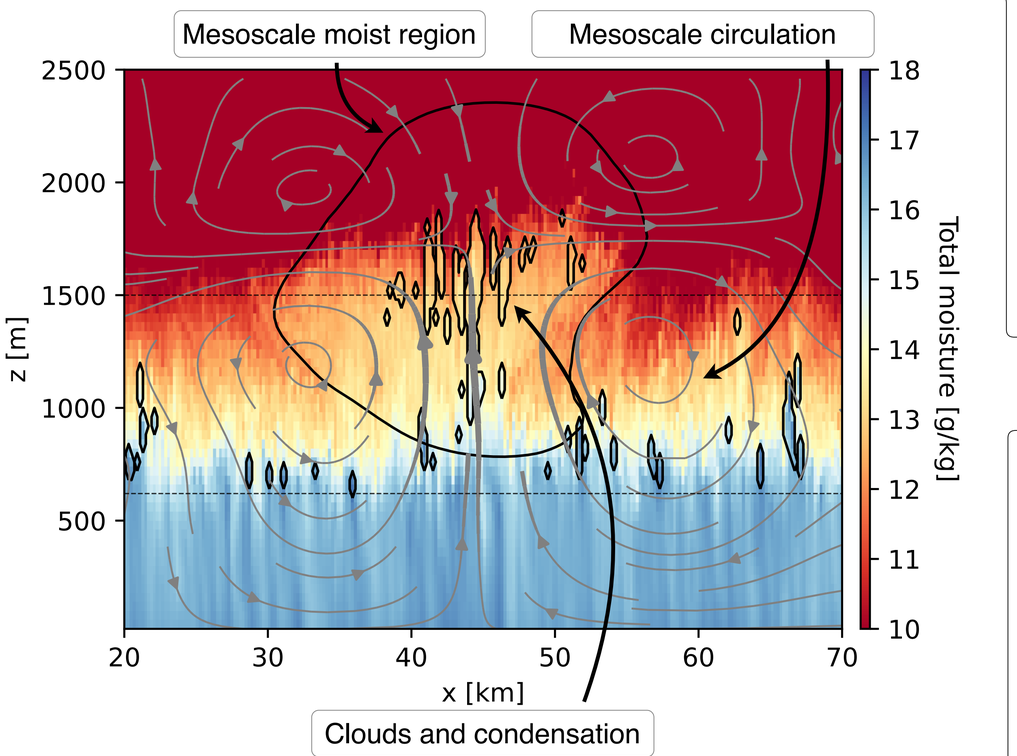

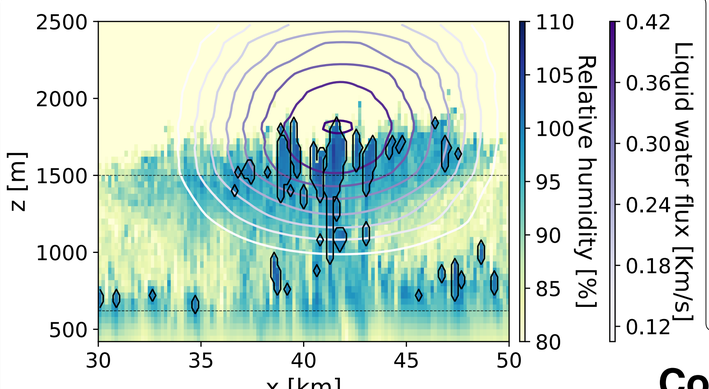

d)

$$\mathcal{C}'_m \propto q'_{t_m}$$

Condensation anomalies $\mathcal{C}'_m$ result from mesoscale **moisture fluctuations** q'_{t_m}

Heat flux anomalies $F'_{\theta_{vl_m}}$ result from **condensation** anomalies $\mathcal{C}'_m$ in clouds at **small scales**

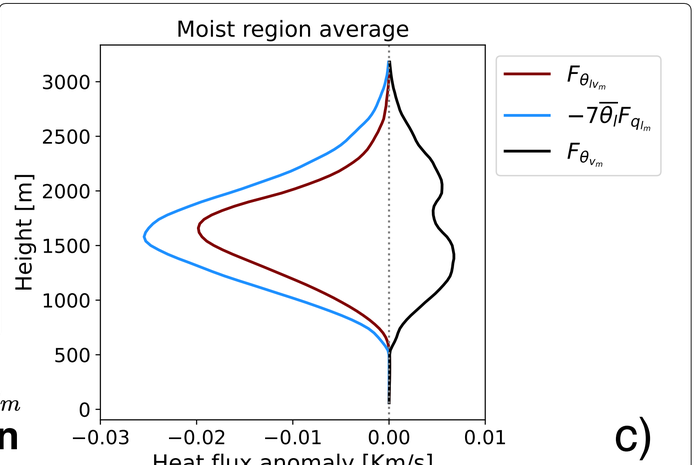

c)

$$\mathcal{C}'_m \approx \partial_z F'_{q_{l_m}}; \quad F'_{\theta_{vl_m}} \approx -7\overline{\theta_l} F'_{q_{l_m}}$$

Figure 2.

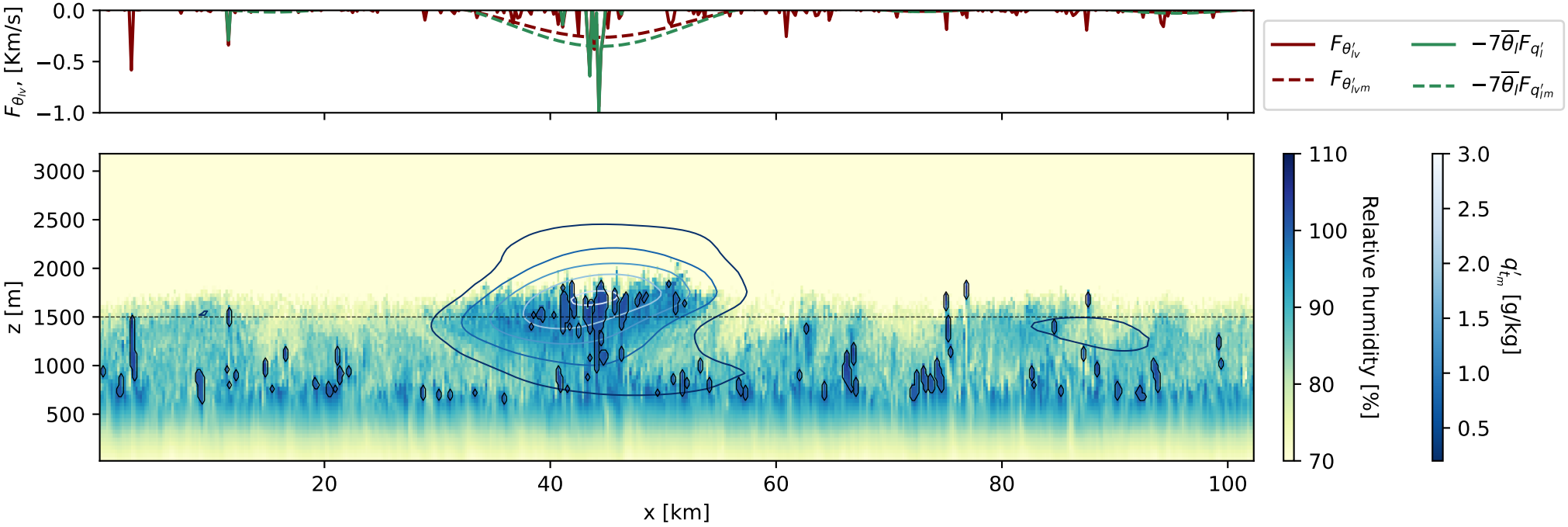
$F_{\theta'_{lv}}$, [Km/s]
0.0
−0.5
−1.0
$F_{\theta'_{lv}}$
$F_{\theta'_{lvm}}$
$-7\overline{\theta}_l F_{q'_l}$
$-7\overline{\theta}_l F_{q'_{lm}}$
z [m]
3000
2500
2000
1500
1000
500
20
40
60
80
100
x [km]
110
100
90
80
70
Relative humidity [%]
3.0
2.5
2.0
1.5
1.0
0.5
q'_{t_m} [g/kg]

Figure 3.

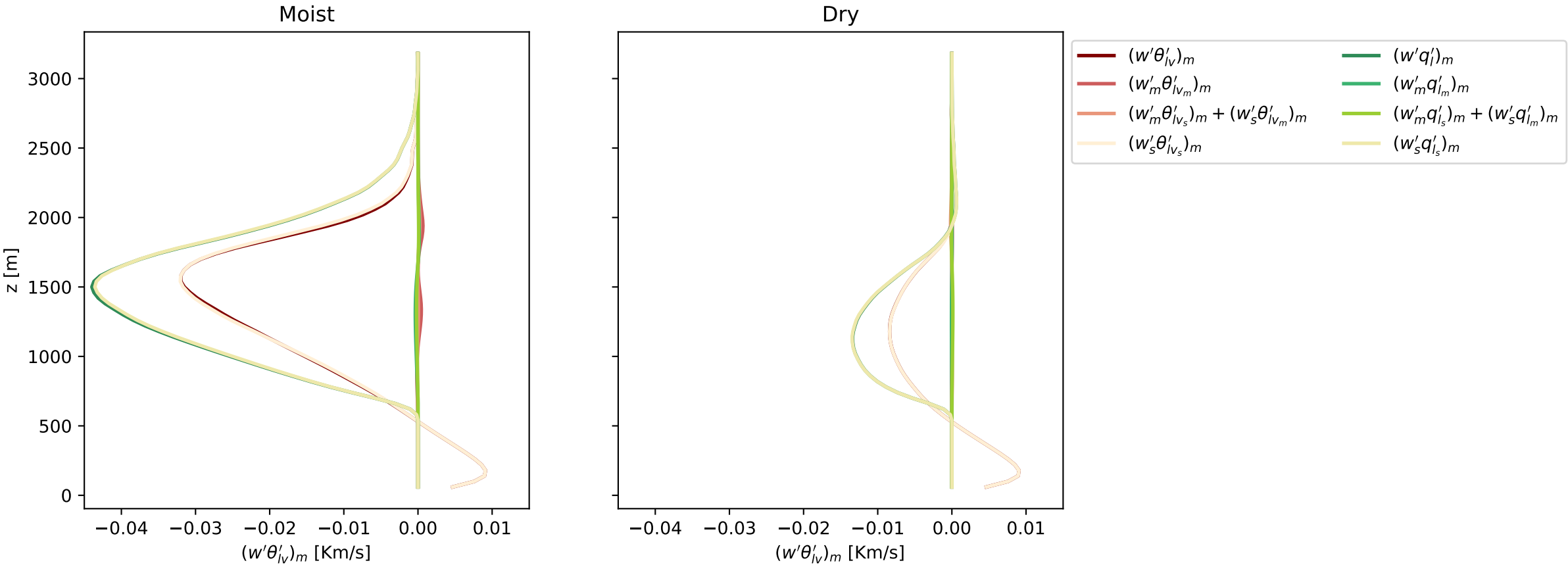
Moist
Dry
z [m]
3000
2500
2000
1500
1000
500
0
−0.04
−0.03
−0.02
−0.01
0.00
0.01
$(w'\theta'_{lv})_m$ [Km/s]
$(w'\theta'_{lv})_m$
$(w'_m\theta'_{lv_m})_m$
$(w'_m\theta'_{lv_s})_m + (w'_s\theta'_{lv_m})_m$
$(w'_s\theta'_{lv_s})_m$
$(w'q'_l)_m$
$(w'_m q'_{l_m})_m$
$(w'_m q'_{l_s})_m + (w'_s q'_{l_m})_m$
$(w'_s q'_{l_s})_m$

Figure 4.

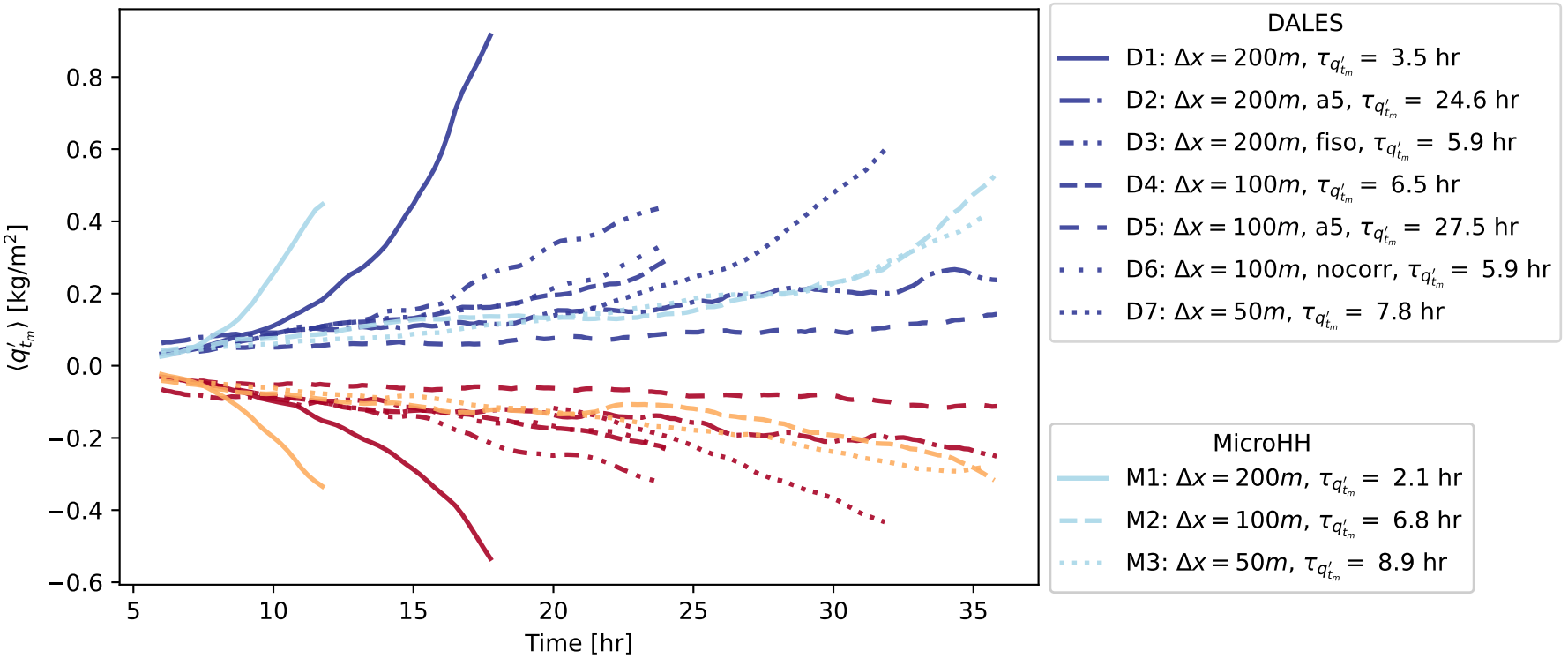
DALES
D1: $\Delta x = 200m$, $\tau_{q'_{t_m}} =$ 3.5 hr
D2: $\Delta x = 200m$, a5, $\tau_{q'_{t_m}} =$ 24.6 hr
D3: $\Delta x = 200m$, fiso, $\tau_{q'_{t_m}} =$ 5.9 hr
D4: $\Delta x = 100m$, $\tau_{q'_{t_m}} =$ 6.5 hr
D5: $\Delta x = 100m$, a5, $\tau_{q'_{t_m}} =$ 27.5 hr
D6: $\Delta x = 100m$, nocorr, $\tau_{q'_{t_m}} =$ 5.9 hr
D7: $\Delta x = 50m$, $\tau_{q'_{t_m}} =$ 7.8 hr
MicroHH
M1: $\Delta x = 200m$, $\tau_{q'_{t_m}} =$ 2.1 hr
M2: $\Delta x = 100m$, $\tau_{q'_{t_m}} =$ 6.8 hr
M3: $\Delta x = 50m$, $\tau_{q'_{t_m}} =$ 8.9 hr
$\langle q'_{t_m} \rangle$ [kg/m^2]
Time [hr]
0.8
0.6
0.4
0.2
0.0
−0.2
−0.4
−0.6
5
10
15
20
25
30
35

Figure 5.

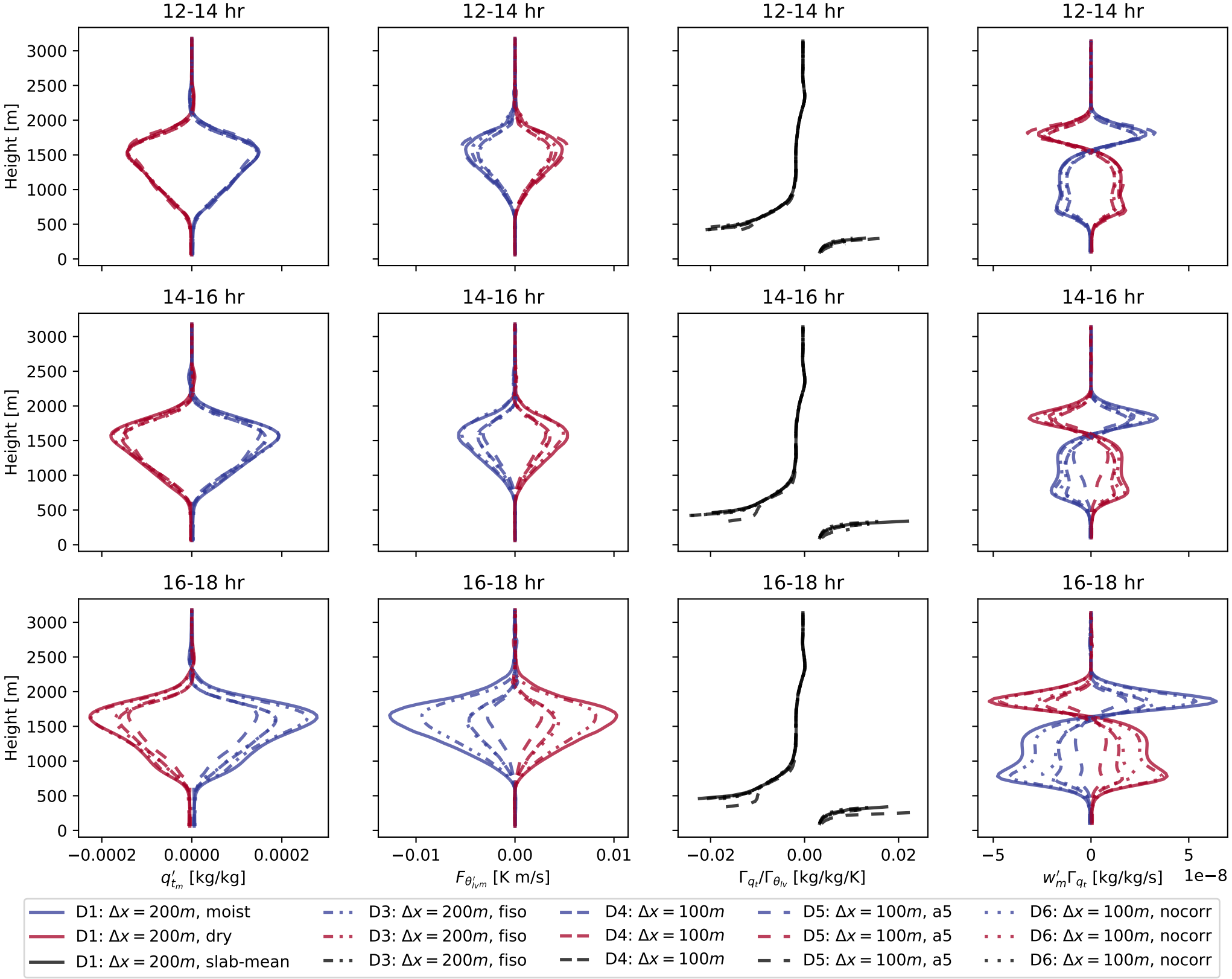
12-14 hr
14-16 hr
16-18 hr
Height [m]
0
500
1000
1500
2000
2500
3000
−0.0002
0.0000
0.0002
q'_{t_m} [kg/kg]
−0.01
0.00
0.01
$F_{\theta'_{lvm}}$ [K m/s]
−0.02
0.00
0.02
$\Gamma_{q_t}/\Gamma_{\theta_{lv}}$ [kg/kg/K]
−5
0
5
1e−8
$w'_m\Gamma_{q_t}$ [kg/kg/s]
D1: $\Delta x = 200m$, moist
D1: $\Delta x = 200m$, dry
D1: $\Delta x = 200m$, slab-mean
D3: $\Delta x = 200m$, fiso
D3: $\Delta x = 200m$, fiso
D3: $\Delta x = 200m$, fiso
D4: $\Delta x = 100m$
D4: $\Delta x = 100m$
D4: $\Delta x = 100m$
D5: $\Delta x = 100m$, a5
D5: $\Delta x = 100m$, a5
D5: $\Delta x = 100m$, a5
D6: $\Delta x = 100m$, nocorr
D6: $\Delta x = 100m$, nocorr
D6: $\Delta x = 100m$, nocorr

Figure 6.

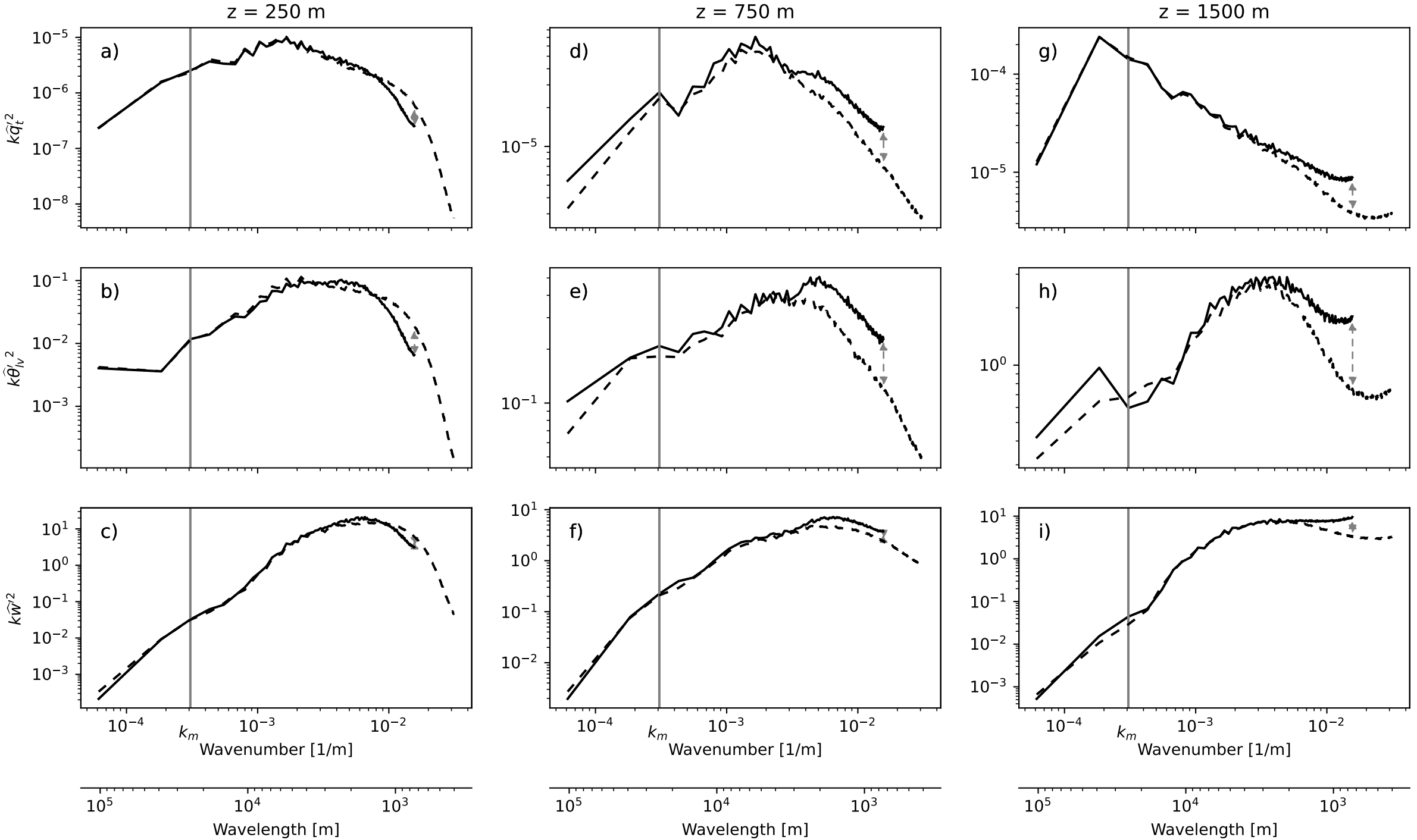
z = 250 m
z = 750 m
z = 1500 m
a)
b)
c)
d)
e)
f)
g)
h)
i)
$k\widehat{q_t'}^2$
$k\widehat{\theta_v'}^2$
$k\widehat{w'}^2$
k_m
Wavenumber [1/m]
Wavelength [m]
D1: $\Delta x = 200m$
D4: $\Delta x = 100m$

Figure 7.

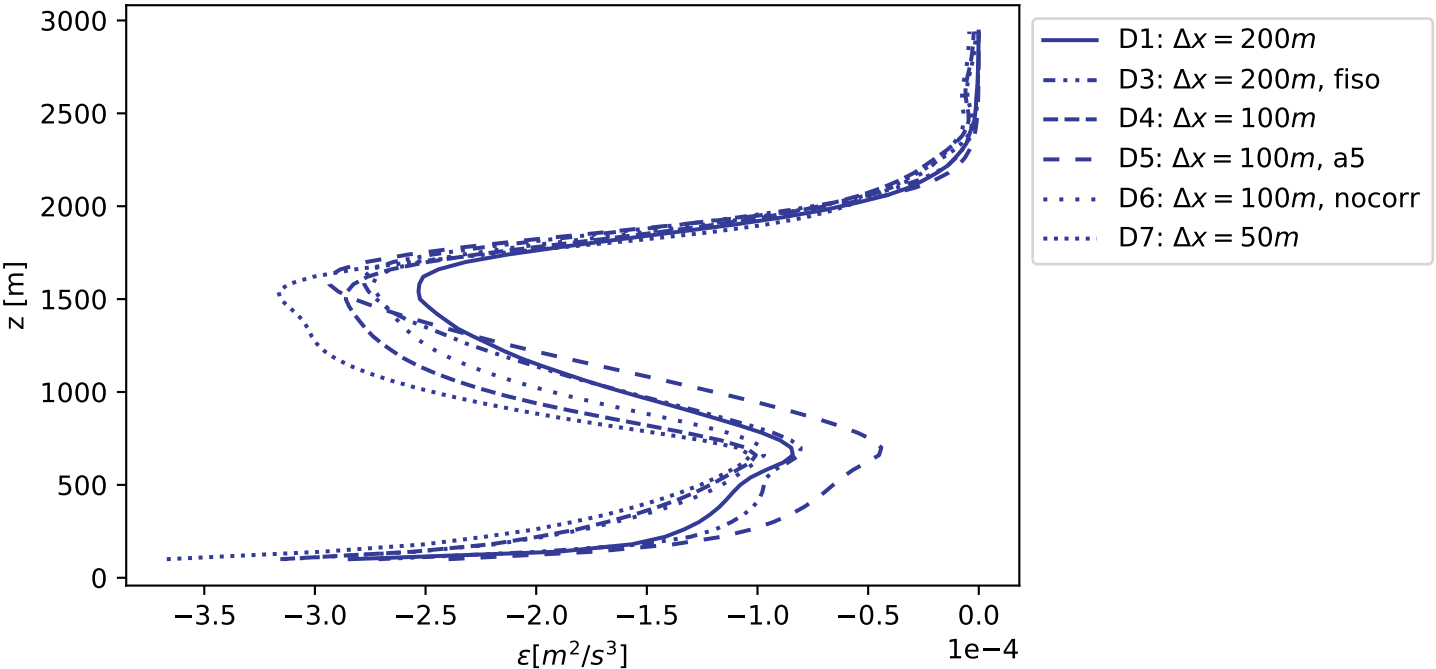
3000
2500
2000
1500
1000
500
0
z [m]
−3.5
−3.0
−2.5
−2.0
−1.5
−1.0
−0.5
0.0
1e−4
$\varepsilon[m^2/s^3]$
D1: $\Delta x = 200m$
D3: $\Delta x = 200m$, fiso
D4: $\Delta x = 100m$
D5: $\Delta x = 100m$, a5
D6: $\Delta x = 100m$, nocorr
D7: $\Delta x = 50m$

Figure 8.

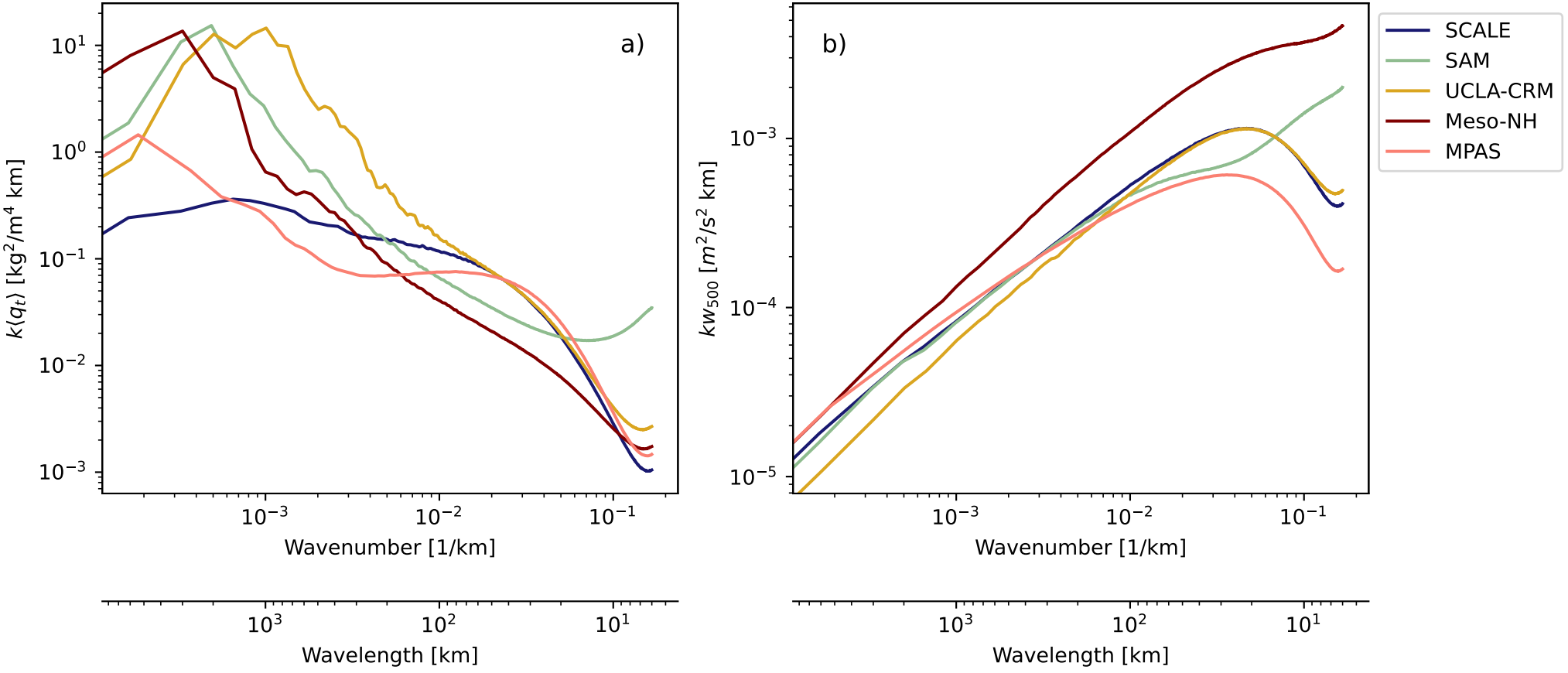
a)
b)
SCALE
SAM
UCLA-CRM
Meso-NH
MPAS
$k\langle q_t \rangle$ [kg^2/m^4 km]
kw_{500} [m^2/s^2 km]
Wavenumber [1/km]
Wavelength [km]
10^{1}
10^{0}
10^{-1}
10^{-2}
10^{-3}
10^{-4}
10^{-5}
10^{3}
10^{2}
10^{1}

Supporting Information for "The time scale of shallow convective self-aggregation in large-eddy simulations is sensitive to numerics"

Martin Janssens[1,2], Jordi Vilà-Guerau de Arellano[1], Chiel C. van Heerwaarden[1], Bart J.H. van Stratum[1], Stephan R. de Roode[2], A. Pier Siebesma[23], Franziska Glassmeier[2]

[1]Wageningen University, Wageningen, Netherlands

[2]Delft University of Technology, Delft, Netherlands

[3]KNMI, De Bilt, Netherlands

Contents of this file

1. Figures S1 to S5

Introduction

In this supplement, we present five figures that support the section "sensitivity to resolution" in the main text. Figs. S1 and S2 show how the three most important terms in the budgets for mesoscale fluctuaions of liquid-water virtual potential temperature (θ'_{lv_m}) and total water specific humidity (q'_{t_m}) are affected by changing the numerical resolution of our simulations. Figs. S3 and S4 display power spectral densities of the three most important variables underlying our simulations' self-aggregation in different numerical configurations run by MicroHH and DALES, respectively. Finally, fig. S5 indicates how dissipation of resolved turbulent kinetic energy is affected by resolution in MicroHH.

References

Bryan, G. H., Wyngaard, J. C., & Fritsch, J. M. (2003). Resolution requirements for the simulation of deep moist convection. *Monthly Weather Review*, *131*(10), 2394–2416.

de Roode, S. R., Siebesma, A. P., Jansson, F., & Janssens, M. (2022). Dependency of mesoscale organization on grid anisotropy in large-eddy simulations. *Under review at Journal of Advances in Modeling Earth Systems (JAMES)*.

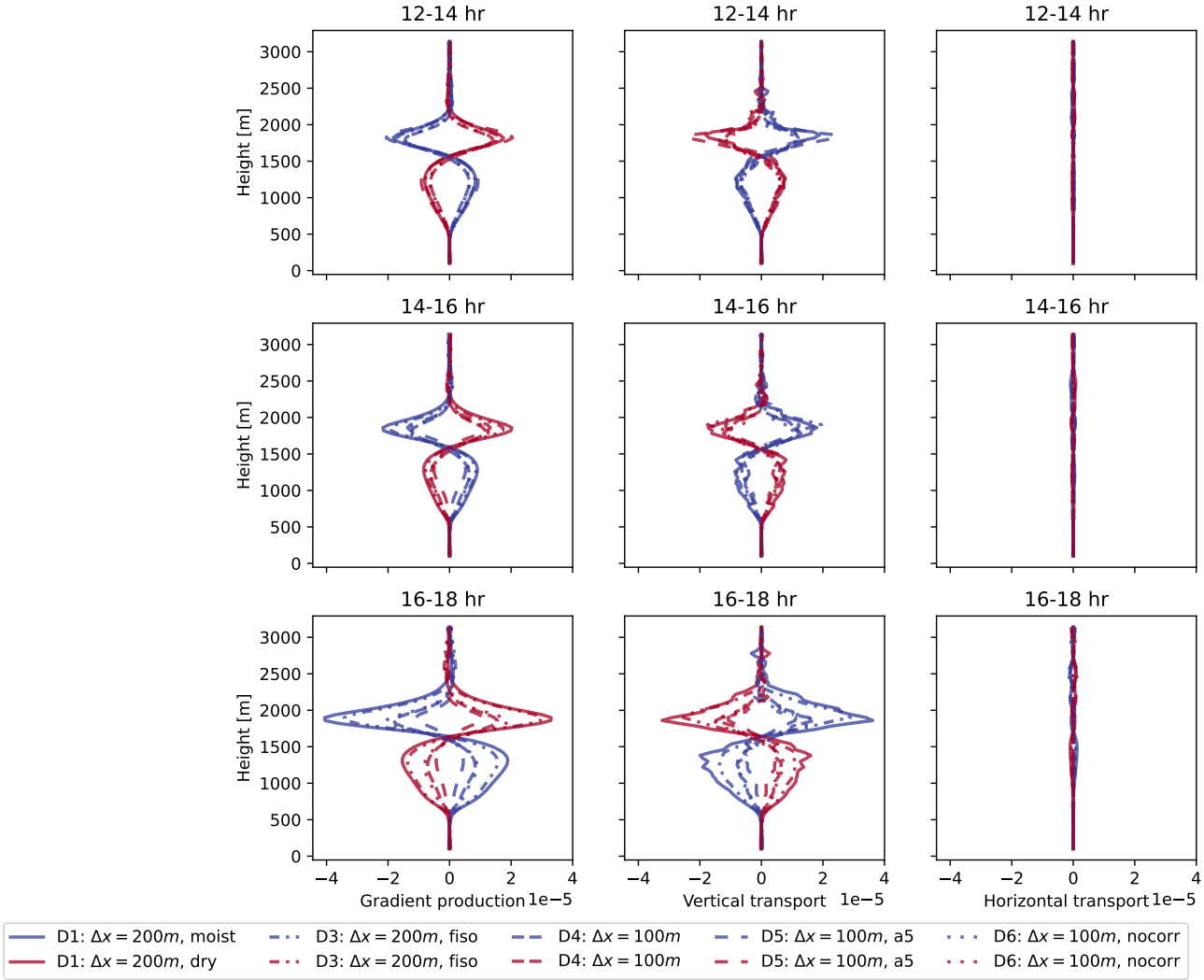

Figure S1. Vertical profiles of gradient production (left), vertical transport (centre) and horizontal transport (right) of θ'_{lv_m} evolving in time (rows) after simulations D1, D3, D5 and D6 have been launched from simulation D4 at $t = 12$ hr. The gradient production of θ'_{lv_m} is almost exactly balanced (up to ensemble averaging deficiencies) by its vertical flux divergence, while horizontal transport remains negligible. Put differently, the weak temperature gradient assumption holds well for all simulations. The upshot is that the numerical sensitivity in gradient production of q'_{t_m}, plotted in fig. S2 and discussed in the main test, can be traced to the increased vigour of the heat flux divergence in coarser simulations, plotted here.

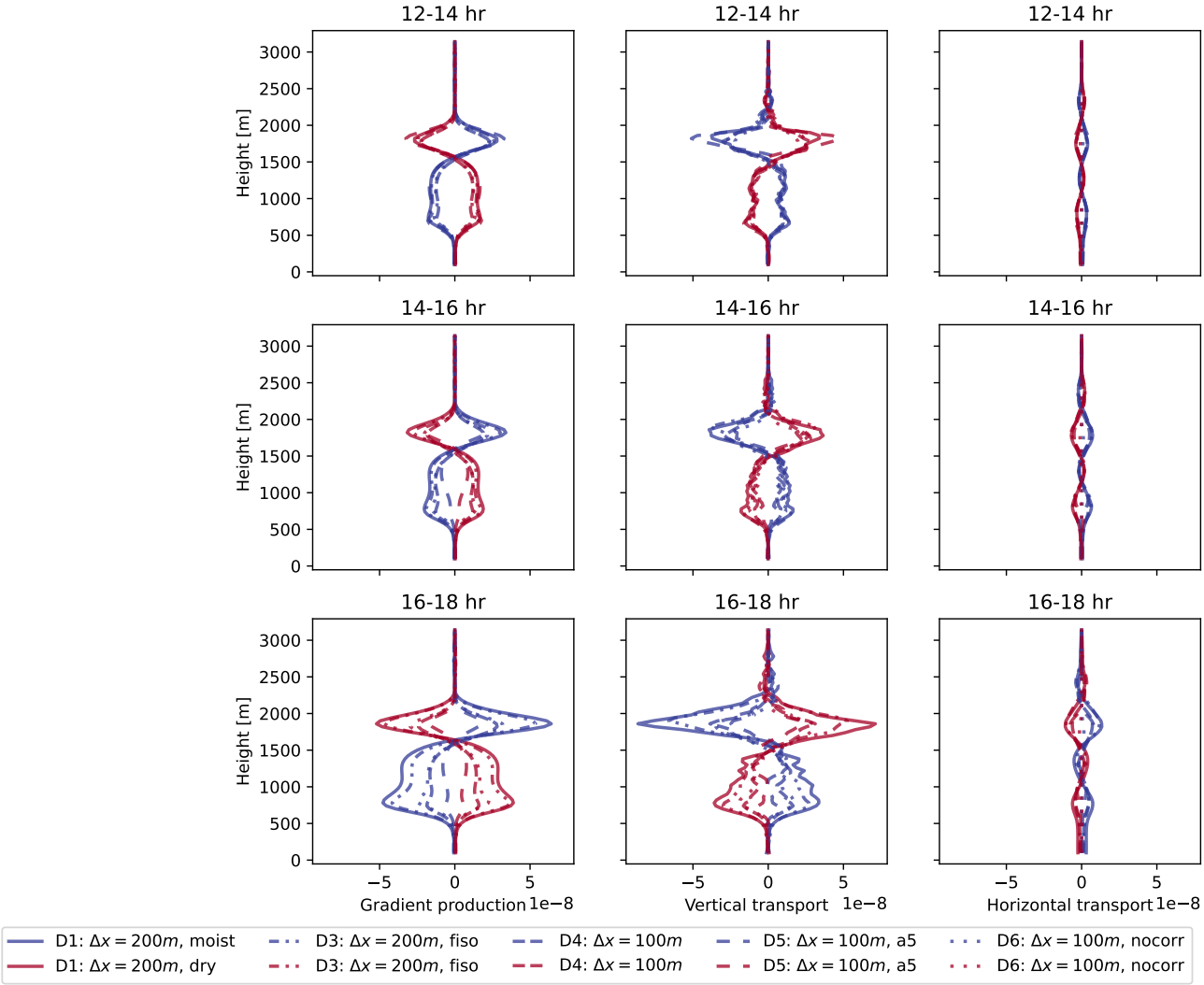

Figure S2. Vertical profiles of gradient production (left), vertical transport (centre) and horizontal transport (right) of q'_{t_m} evolving in time (rows) after simulations D1, D3, D5 and D6 have been launched from simulation D4 at $t = 12$ hr. Both the gradient production (which comes about through heat flux divergence, see fig. S1) and the vertical flux divergence intensify in coarser simulations, with exception of D5, which runs with a diffusive advection scheme that slows the growth. Horizontal moisture advection is small and unaffected by resolution change, i.e. quicker q'_{t_m} growth in coarser simulations is not because they mix moisture variance horizontally and to smaller scales less efficiently, but because they produce it more efficiently.

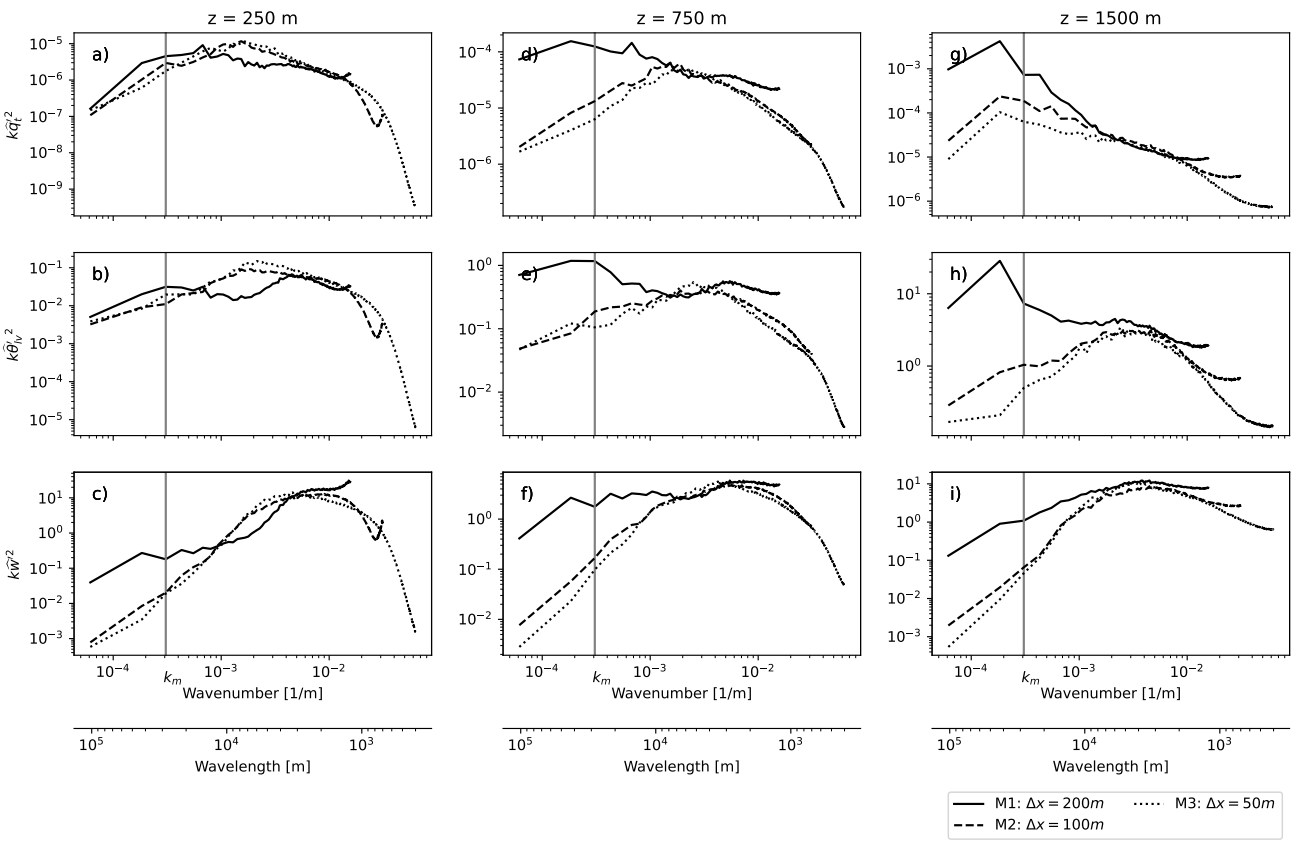

Figure S3. Radial power spectral density of q_t ($k\widehat{q_t'}^2$, a, d, g) θ_{lv} ($k\widehat{\theta_{lv}'}^2$, b, e, h) and w ($k\widehat{w'}^2$, c, f, i) for simulations M1-M3, i.e. at increasingly fine grid spacing, over x-y cross-sections at 250m (a-c, in middle of sub-cloud layer), 750m (d-f, in cloud layer) and 1500m (g-i, at inversion base). k_m indicates the wavenumber that separates the mesoscales from the sub-mesoscales. The spectra are plotted after 12 hours of simulation without restart, i.e. these spectra subsume historical information of their self-generated state, such that the excess variance predicted for the coarsest simulation (M1) is in part due to its advanced, self-reinforcing scale growth. Note, however, the same spectral variance plateaus at all three simulations' smallest, resolved scales at their inversion base, though it shifts to increasingly small, quiescent and thus inconsequential scales.

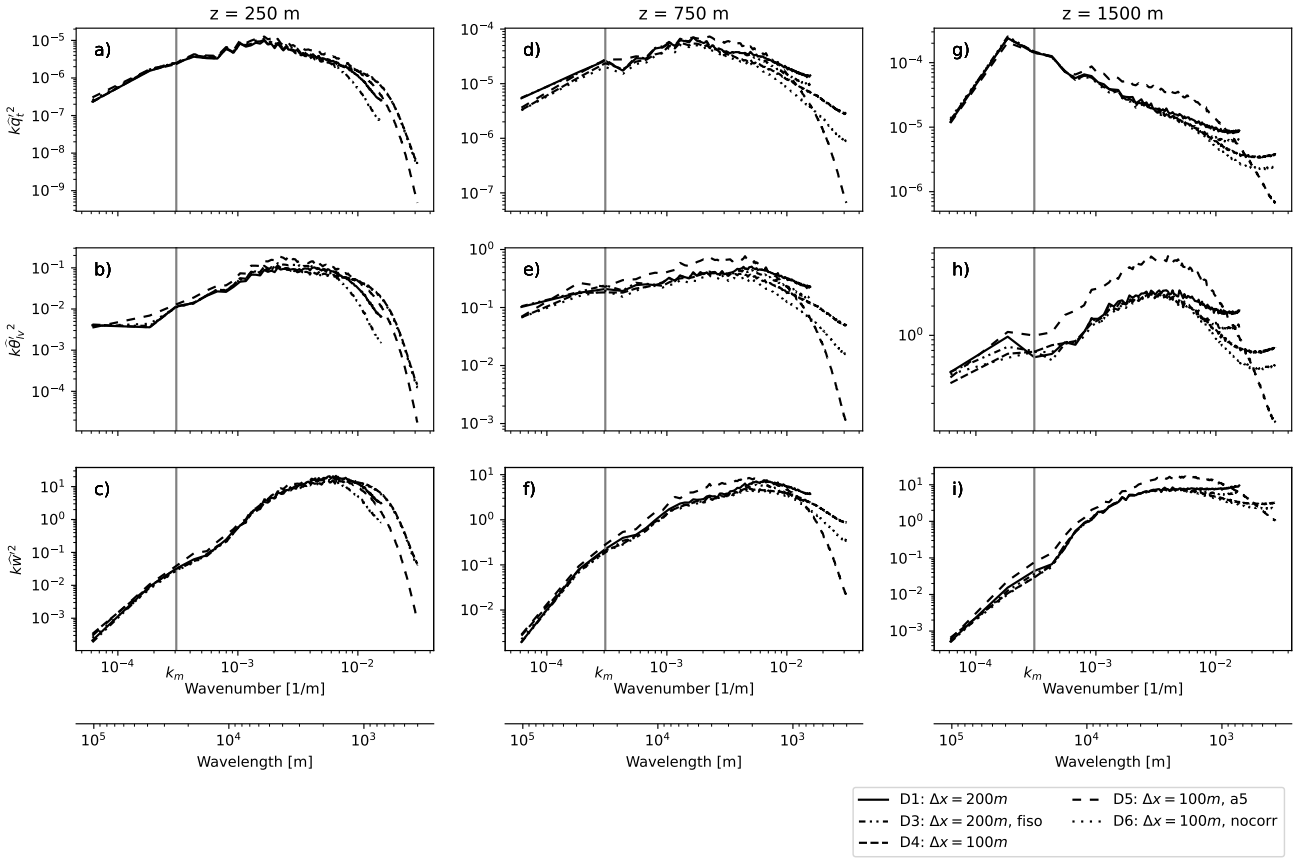

Figure S4. As fig. S3, for the three DALES simulations D1, D3 and D5 restarted from simulation D4, averaged over the first hour after the restart. The more diffusive simulations (D3 and D5) possess a reduced variance plateau at their smallest, resolved scales with respect to D1, slowing their self-aggregation. Simulation D5 appears to compensate for a lack of variability in its smallest scales - at $\Delta x = 100$m any variance < 500 m is controlled by free parameters of the numerical scheme (Bryan et al., 2003) - by shifting variance to larger scales, perhaps following the mechanism suggested by de Roode et al. (2022). Note that its overall variance in the sub-mesoscales remains smaller than that of its 2nd order advective counterpart D4, especially in the cloud layer.)

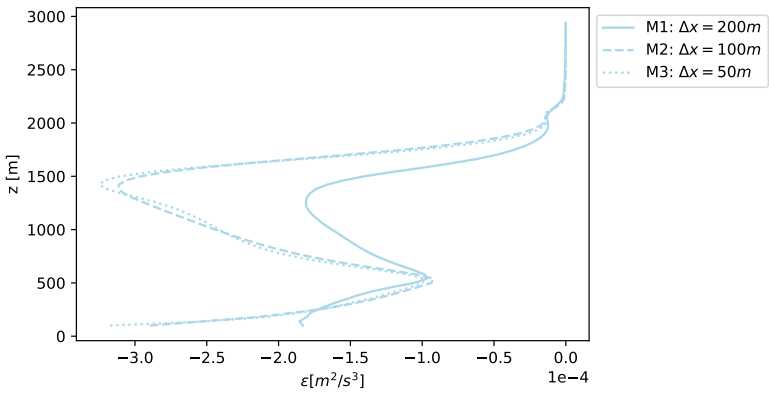

Figure S5. Profiles of dissipation ε of resolved turbulent kinetic energy e, averaged between 3-5 hr, for numerical configurations indicated by the line styles, in simulations run by MicroHH, i.e. before any of the simulations have self-aggregated appreciably. ε is much smaller in simulation M1 than in M2 and M3, consistent with this simulation being underdissipated and self-aggregating much more rapidly than its finer counterparts. Encouragingly, M2 and M3 differ less, though M2 remains underdissipated, especially at inversion base where scale growth is maximised.